Technical Report

TR-08-12

Inspection of copper canister for spent nuclear fuel by means of ultrasound

FSW monitoring with emission, copper characterization and ultrasonic imaging

Tadeusz Stepinski (editor), Marcus Engholm,
Tomas Olofsson
Uppsala Univerity, Signals and Systems,
Department of Technical Sciences, Sweden

September 2008

Svensk Kärnbränslehantering AB
Swedish Nuclear Fuel
and Waste Management Co
Box 250, SE-101 24 Stockholm
Tel +46 8 459 84 00

Inspection of copper canister for spent nuclear fuel by means of ultrasound

FSW monitoring with emission, copper characterization and ultrasonic imaging

Tadeusz Stepinski (editor), Marcus Engholm,
Tomas Olofsson
Uppsala Univerity, Signals and Systems,
Department of Technical Sciences, Sweden

September 2008

Abstract

This report contains the research results concerning advanced ultrasound for the inspection of copper canisters for spent nuclear fuel obtained at Signals and Systems, Uppsala University in 2007.

In the first part of the report we further develop the concept of monitoring of the friction stir welding (FSW) process by means of acoustic emission (AE) technique implemented using multiple sensors formed into a circular array. After a brief introduction into the field of arrays and beamforming we focus on the features of uniform circular arrays (UCA). Results obtained from the simulations of UCA beamformer based on phase mode concept are presented for the continuous wave as well as for the pulse, noise-free input signals. The influence of white noise corrupting the input pulse is also considered and a simple regularization technique proposed as a solution to this problem.

The second part of the report is concerned with aspects related to ultrasonic attenuation of copper material used for canisters. We compare resonant ultrasound spectroscopy (RUS) with other methods used for characterization of the copper material. RUS is a non-destructive technique based on sensing mechanical resonances present in a tested sample in the ultrasonic frequency range. Resonance frequencies observed in a material sample (with given geometry) are directly related to the vibration modes occurring in the inspected volume defined by the material parameters (elastic constants). We solve the inverse problem that consists in using the information about resonance frequencies acquired in physical measurements for estimating material parameters. Our aim in this project is to investigate the feasibility of RUS for the grain size estimation in copper using copper specimens that were provided by SKB.

In the final part we consider the design of input signals for ultrasonic arrays. The Bayesian linear minimum mean squared error (LMMSE) estimator discussed in our former reports is studied. We show that it offers a useful tool for designing and evaluating ultrasonic array systems. In particular, a method to design input signals, driving an array system, so that the expected error of the LMMSE estimator is minimized for chosen set of control points is introduced.

Contents

Chapter 1

Introduction

by Tadeusz Stepinski

In this report we are presenting our recent research results concerning ultrasonic inspection of copper canisters for spent nuclear fuel.

Our research activity in this project in 2007 was split into three separate tasks which are reported in the following separate chapters:

- FSW process monitoring,
- Grain size estimation resonant ultrasound spectroscopy,
- High resolution synthetic aperture imaging.

The first chapter deals with the feasibility of the FSW process monitoring technique based on acoustic emission and phased array techniques. In our recent report (TR-06-47) we proposed a new solution to the FSW monitoring problem using a uniform circular array (UCA) that can be focused on a certain zone at the canister's circumference. The array placed in the middle of the canister lock (in the future possibly integrated in the FSW machine) will receive the acoustic emission signals bearing the information about the state of the FSW process and the tool condition. The aim is to detect an abnormal progress of the FSW process as well as to monitor the tool wear. This will be preformed by the UCA that will be focused by electronic means on the interesting part of the lid circumference. In the present step we have continued the UCA development to prepare laboratory tests using our multi-channel ultrasonic system for recording acoustic emission events in a circular test disc.

In the second chapter we investigate feasibility of ultrasound resonance spectroscopy as a tool for quantitative characterization of grain size in copper material used for SKB's canisters. A number of ultrasonic techniques aimed at grain structure characterization were presented in our former reports (TR-99-12, TR-99-43, TR-00-23 and TR-06-02). We have investigated the indirect techniques based on attenuation measurement, the independent scattering model, and K-distribution. It appeared, however, that none of those techniques produced results that were clearly correlated with the grain size data obtained using classical optical measurements. Here, we investigate resonant ultrasound spectroscopy (RUS), which is a non-destructive technique based on sensing mechanical resonances present in a tested sample in the ultrasonic frequency range. In a broadband resonance spectroscopy the frequency response of the inspected sample is measured using two (or more) specially designed ultrasonic transducers. Resonance frequencies observed in a material sample (with given geometry) correspond to the vibration modes occurring in the inspected volume defined by the material parameters (elastic constants). The information about resonance frequencies present in a predefined frequency band can be used for estimating material parameters or detecting defects. Our aim in this project is to investigate the feasibility of RUS for the grain size estimation in copper using copper specimens that have been provided by SKB. The specimens that have a well-defined geometry are characterized by different grain size ranging from 50μm to 510μm. In the first step of this project we have developed the theoretical model estimating resonance frequencies corresponding to different vibration modes present in a solid parallelepiped. We also developed a suitable test setup that consists of a pair of piezoelectric transducers, a preamplifier and the Agilent Network Analyzer. In the present stage we report experiments consisting in the acquisition of resonance spectra for a number of copper samples and estimating the elasticity constants based on those measurements. Correlation between the estimated elasticity constants and ultrasonic attenuation as well as grain size is evaluated.

In the final chapter we propose a method for optimizing signals used for ultrasonic imaging using phased arrays. Traditional beamforming techniques for ultrasonic arrays are based on spatial filtering of array data to obtain a sharp image of the scattering objects. Beamforming using the classical time-domain delay-and-sum method mimics an acoustical lens. First, the

array elements are excited by pulses that provide focus effect in a desired zone. Second, the received signals are processed by delay-line operations in real time or using post-processing, for instance, in synthetic aperture systems. Since modern array systems allow for excitation of separate elements using arbitrary waveforms we investigate a new method that consists in optimizing the input signals to an ultrasonic array according to an imaging task at hand. This means that we aim at illuminating a number of control points in the medium in a way that creates optimal conditions for imaging the targets present in those points. In other words, we will create an acoustic field with several focal points in front of the array.

Chapter 2

Uniform Circular Arrays for Acoustic Emission

by Tadeusz Stepinski

2.1 Introduction

Feasibility of the friction stir welding (FSW) process for sealing SKB's copper canisters has been demonstrated at SKB's Canister Laboratory at Oskarshamn. The FSW process is relatively robust and normally yields flawless welds. However, in some conditions (e.g., when the tool is excessively worn out) flaws may be produced that are very difficult to detect using ordinary nondestructive methods. Structural characterization shows that the tool wear interferes with the weld quality and accounts for the formation of voids in the nugget zone [1]. Therefore, to assure weld quality a real-time monitoring of the FSW process would be highly desired.

Recently, the use of acoustic emission (AE) for that purpose has been reported. Zeng *at al* [1] reports the results showing that the AE sensing provides a potentially effective method for the on-line monitoring of tool wear. They have shown that the increased tool wear is indicated by the the higher amplitudes the AE events recorded from the FSW weld. Yoon *at al* [2] also present results showing that in-process real-time FSW weld quality evaluation (such as strength and ductility) can be performed using acoustic emission.

In our former report [3] the concept of monitoring of the friction stir welding process by means of acoustic emission was proposed. This concept was further developed in the diploma project performed by K.Dahlgren. This chapter contains an edited version of the Dahlgren's diploma report [4].

Two main sources of AE signals are of interest when monitoring the FSW process used for copper canisters welding:

- the high intensity continuous emission generated by the FSW tool itself, and
- the low intensity burst emissions generated due to local energy releases inside the material under stress.

It would be highly desirable to separate these two sources so that the signals of interest can be detected. Our proposed solution is to use an omnidirectional *array* of multiple sensors that can be steered electronically to detect signals from a specific direction. In this case, for reasons that will be explained below, a circular array will be used. The proposed setup of the monitoring system is shown in Fig. 2.1.

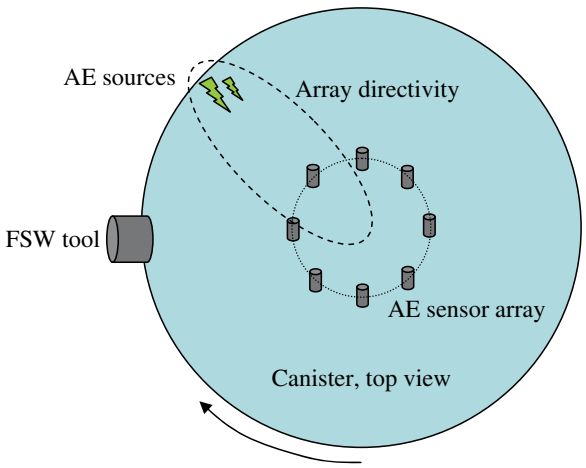

Figure 2.1: Configuration of the AE monitoring system for the FSW of the copper canisters.

2.2 Introduction to Arrays

An array is a group of sensors in which the phase of an incoming signal at the respective sensors is varied so that the radiation pattern is reinforced in a desired direction and suppressed in other directions. This technology was originally developed during World War II for early radar systems. Since then, it has been adapted for many other applications.

The array configuration describes the physical characteristics of the array. It can be broken down into two parts. The first part is the antenna pattern of the individual elements of the array. The antenna pattern of an isotropic element is uniform in all directions. We assume all elements are isotropic. The second part of the array configuration is the array geometry. This denotes the physical position of the elements, they can be arranged in any shape, but they can all be divided into three categories: linear, planar and volumetric. The shape and size of the array, as well as the spacing of the elements affects the characteristics of the array.

2.2.1 Arrays and Spatial Filters

An array is used to filter signals by exploiting their spatial characteristics. Usually, it is desired to construct the array so that signals from a particular angle of interest are enhanced by constructive interference and signals from other angles are rejected by destructive interference. Designing arrays to achieve desired performance involves trade-offs between many parameters, such as the geometry of the array, the number of sensors, the angular resolution, and signal-to-noise ratio, sidelobe levels, and a number of other factors.

Two basic aspects that determine the performance of arrays are the geometry and the element weightings. The geometry establishes several constrains of their operation. For example, a linear array provides information of source bearing relative to the array axis. However, a planar array is required if estimates of both azimuth and elevation are needed. The geometry is often limited by physical constraints of the area of interest. The design of the weightings of the data at each sensor output determines the spatial filtering characteristics of the array for a given geometry. By using different weightings, the *beampattern* formed by the array can be drastically altered.

This report will describe arrays and their characteristics using a spherical coordinate system. The relationships between rectangular and spherical coordinates are:

$$
\begin{aligned}
x &= r \sin\theta \cos\phi \\
y &= r \sin\theta \sin\phi \\
z &= r \cos\theta
\end{aligned}
$$

The full set of coordinates is shown in Fig. 2.2.

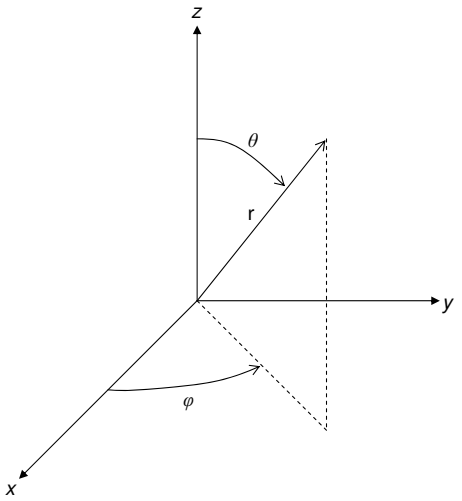

Figure 2.2: Spherical coordinate system

2.3 Beamforming

Beamforming is a method of enhancing signals from a specific direction in space while at the same time attenuating disturbing signals arriving at the array from other directions. This has many applications in many different areas, such as radio-communications, medicine, astronomy and military devices.

Assume that an array with n elements with elements positioned at $\mathbf{p}_n$ receives an incoming signal $x(t)$ from the direction $\mathbf{a}$. The direction $\mathbf{a}$ is defined by two angles, the azimuth angle ϕ, and the elevation angle θ.

$$\mathbf{a} = -\begin{bmatrix} \sin\theta\cos\phi \\ \sin\theta\sin\phi \\ \cos\theta \end{bmatrix}$$

The minus sign is due to the direction of $\mathbf{a}$.

A complex signal $x(t)$ can be regarded as a sinusoidal pulse modulated signal,

$$x(t) = e^{j\omega t}.$$

The received signals that propagate through the medium as plane waves with velocity c and angular frequency ω are considered to originate at a distance large enough from the array that the wave fronts are planar at the array. The signal received at each sensor in the array will be

$$x_n(t) = e^{j(\omega t - k\mathbf{p}_n^T\mathbf{a})} \quad \text{for } n = 0, \ldots, N-1,$$

where k is the *wavenumber* associated with the plane wave ($k = \omega/c$). The result of a simple summation of the outputs of the N sensors of the array gives the scalar beamformer output $y(t)$. This is generally defined as

$$y(t) = \mathbf{w} \cdot x_n(t),$$

where the vector **w** is a weight vector. For the simple summing mentioned, the elements of the this vector are equal. By operating on the sensor outputs with different weight vectors, the array beampattern can be altered [5].

2.3.1 Beamsteering

Assume that an arbitrary array with N elements receives an incoming signal from a specific direction **a**. By introducing time delays to the individual elements of the array before summing, the signal from the desired direction can be summed coherently. This is called *steering* the array to a specific direction.

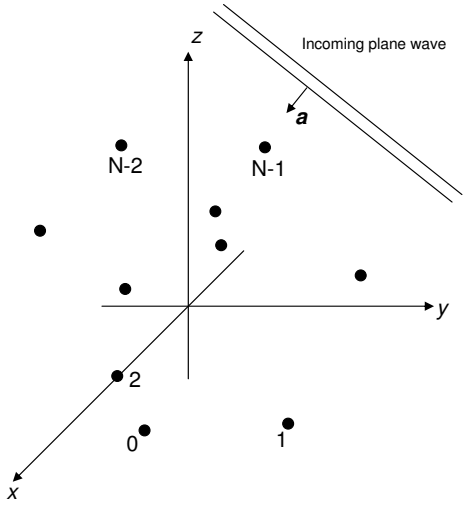

Figure 2.3: Arbitrary N-element array with incoming plane wave.

An example of a simple beamforming operation is the delay-and-sum beamformer. Assume we want the array to focus on a specific direction **a**. An incoming signal with frequency w from this direction will reach the elements in the array at different times. The situation is shown in Fig. 2.3. By delaying each channel before summing, it is possible to enhance the strength of a signal received from the desired direction. For narrow-band signals, in the frequency domain, time delays are equal to a phase shift. If $x(t)$ is the signal that would be received at the origin of the system, then the signal received at the elements at their respective positions $\mathbf{p}_n$ is

$$\mathbf{x}(t, \mathbf{p}) = \begin{bmatrix} x(t-\tau_0) \\ x(t-\tau_1) \\ \vdots \\ x(t-\tau_{N-1}) \end{bmatrix},$$

where

$$\tau_n = \frac{\mathbf{a}^T \mathbf{p}_n}{c}$$

is the time delay applied to the element n, c is the propagation velocity in the medium and **a** is the direction defined above.

By introducing these time delays in the respective element channel before summing, signals from the direction **a** are summed coherently and, therefore, the beamformer output is reinforced

significantly compared to that produced for the signals from other directions. Principle of the delay-and-sum beamformer is shown in Fig. 2.4. The normalizing factor $1/N$ is included to obtain unity gain [5], [6].

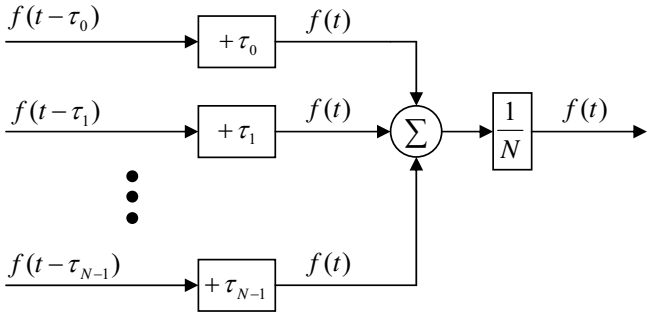

Figure 2.4: Scheme of a delay-and-sum beamformer.

In many applications, simply adding the sensor outputs coherently is not enough to achieve the desired performance. In the beamforming example above, the weights of the elements are uniform and equal to $1/N$. By using different weights of the elements before summing, the beampattern of the array can be altered to meet a desired performance requirement. This process is called array apodization.

2.3.2 Beampattern

When an array is steered along a direction **a** for enhancing signals originating from that specific direction, the array will still receive signals from all other directions. Assume that the array is designed for detecting signals from **a** with a specific angular frequency ω_c. How will the array respond if the signal did not originate from **a**, but from another direction?

The *beampattern* for an array is defined as the response from the array for signals with a specific wavenumber for all directions. This is a very important characteristic of the array. Much information of the performance of the array can be gathered from its beampattern.

The beampattern is often plotted as the *beam power* versus direction, where the beam power is the power of the beam as a function of the incident angle. The standard is to use a logarithmic scale for the beam pattern.

Beampattern Parameters

From the beampattern of an array, valuable information can be gathered. The most important features are (cf Fig 2.5):

- 3-dB beamwidth (the half-power beamwidth)
- Distance to the first null
- Height of the first sidelobe
- Distance to grating lobes

For a more thorough description of the parameters, see Van Trees [6].

In the sequel we will mostly deal with two of these parameters, namely, the 3-dB beamwidth and the height of the first sidelobe. These are two very important parameters of an array.

The 3-dB beamwidth is a measure of the width of the beam. It is defined as the beamwidth between the points where the amplitude of the beam are 3dB lower than the maximum. This is a measure of the lateral resolution of the array. If the 3-dB beamwidth is too large, the array will be unable to differentiate two signals originating from the close directions.

The height of the sidelobes is a measure of how much signals from other directions will affect the output of the array. Ideally, the sidelobe levels should be very low.

An excerpt from the beampattern of a uniform linear array (more on them later) with 20 elements and uniform weighting steered to broadside is shown in Fig. 2.5 together with the 3-dB beamwidth and sidelobe level definitions.

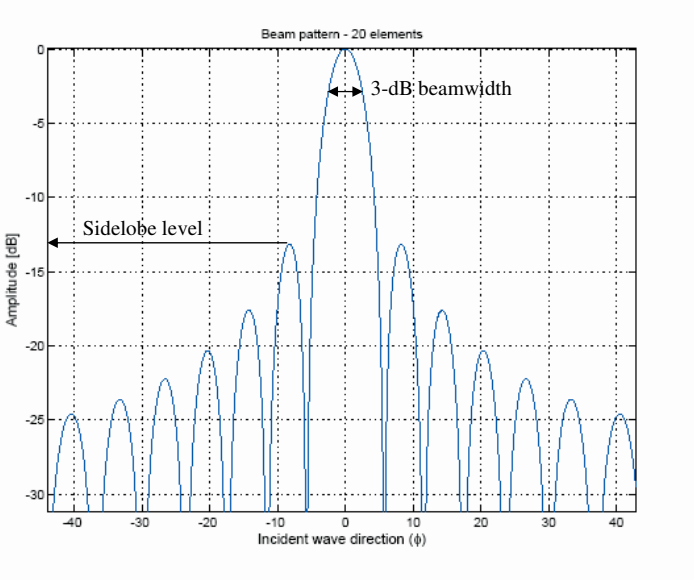

Figure 2.5: 3-dB beamwidth and sidelobe levels for a 20 element uniform linear array.

The 3-dB beamwidth and sidelobe levels are closely related. Apodization coefficients are used to control these parameters. Generally, by lowering the sidelobes to attenuate signals from unwanted directions, the width of the main lobe increases, so that the spatial resolution is lowered.

The most commonly used array type are linear arrays. A linear array consists of N elements positioned on a line in space. If the the separation (pitch) d between all the elements of a linear array is the same it is said to be an *uniform linear array*(ULA).

2.4 Circular Arrays

Compared to linear arrays, circular arrays are less used in practical applications although they offer several features over linear arrays. Firstly, due to the 2D planar geometry of a circular array a circular array can be used to detect both the azimuth and the elevation of the signal source. Secondly, circular arrays have 360° azimuth coverage, and the shape of the beam in the plane of the array (azimuth plane) is essentially unchanged for all steering directions [7].

However, it is not possible to directly weight the outputs of the sensors in a circular array to control the sidelobe height, as in the case of linear arrays. This leads to some difficulties with beamforming design and special tools are required to achieve the desired beampattern. This will be reviewed in the following sections.

2.4.1 Uniform Circular Arrays

The geometry of a *uniform circular array (UCA)* is shown in Fig. 2.6. A UCA has equal angular spacing γ_c between all elements. All discussion and simulations below will consider UCA's.

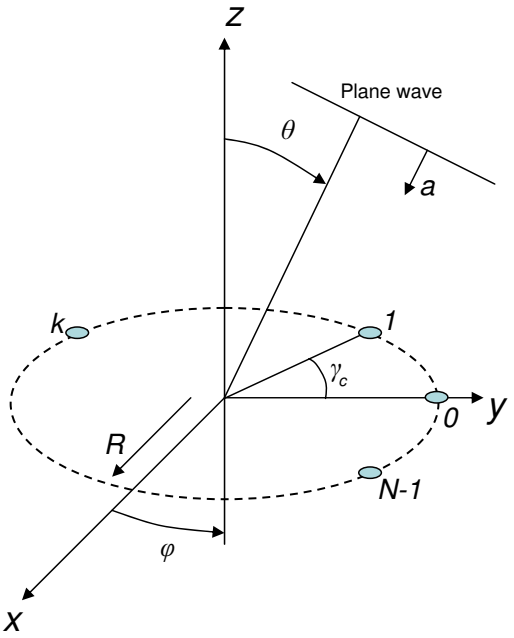

Figure 2.6: Geometry for a uniform circular array in the xy-plane.

Consider an incoming plane wave with wavenumber k_0 propagating in the direction $\mathbf{a}$. Element n of the UCA is positioned at

$$\mathbf{p}_n = (R\cos(n-1)\gamma_c, R\sin(n-1)\gamma_c, 0)$$

where R is the radius of the array. The array manifold vector for a UCA is therefore

$$\mathbf{v_k}(\mathbf{k}) = \begin{bmatrix} e^{-j\mathbf{k}^T\mathbf{p}_0} \\ e^{-j\mathbf{k}^T\mathbf{p}_1} \\ \vdots \\ e^{-j\mathbf{k}^T\mathbf{p}_{N-1}} \end{bmatrix} = \begin{bmatrix} e^{jk_0R\sin\theta\cos(\phi)} \\ e^{jk_0R\sin\theta\cos(\phi-\gamma_c)} \\ \vdots \\ e^{jk_0R\sin\theta\cos(\phi-(N-1)\gamma_c)} \end{bmatrix}. \tag{2.1}$$

However, contrary to the ULA the array manifold vector cannot be directly used to synthesize a desired beampattern for an UCA. Instead, a technique called *phase mode excitation* is used.

Phase Mode Excitation for UCA

Phase mode excitation of UCA's, which is essentially Fourier analysis of the array excitation function, was first studied by researchers in the early 1960's. This theory resulted in a pattern synthesis technique for UCA's using techniques normally associated with linear arrays [8].

Phase mode excitation-based beamforming synthesizes a virtual beamspace manifold similar to that of a ULA by transforming the UCA into a virtual array for which the spatial response is similar in form (Vandermonde structure) to that of a ULA. By operating on the virtual array manifold, it is possible to achieve the desired beam pattern for the uniform circular array by (among others) using the weighting method normally used for ULA's. The transformation involves a matrix network known as *Butler matrix* in which phase shifters are coupled to several elements simultaneously.

It was also discovered that the Butler matrix was closely related to the Discrete Fourier Transform (DFT). It can be shown that using the Butler matrix, any arbitrary excitation of a UCA can be expressed by a spatial Fourier series, in which each term constitutes an *excitation function*, referred to as *phase mode*, whose phase changes by uniform steps from element to element as in the beam excitation of a linear array [3].

Beamforming Matrices and Manifold Vectors

It was shown in our former report [3] that the phase mode excitation beamformer takes the form of a linear transformation of the input vector $\mathbf{x}(k)$ in the following form

$$y(k) = \mathbf{w}_{PM}^H \mathbf{B}_{PM}^H \mathbf{x}(k). \tag{2.2}$$

where $\mathbf{B}_{PM}^H$ is the Butler matrix and $\mathbf{w}_{PM}^H$ is the weighting vector. The phase mode excitation beamformer has the structure shown in Fig. 2.7.

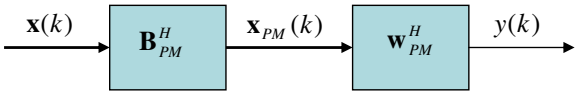

Figure 2.7: Scheme of a phase mode excitation beamformer.

Array Steering

An advantage of the UCA is that the shape of the beampattern in the azimuth plane is essentially unchanged when steering the array in different directions, compared to the steering of a ULA, where the resolution is lowered the farther away from broadside it is steered. The UCA also has 360° azimuth coverage, compared to a ULA which has a (theoretical) coverage of 180°. Another advantage of the UCA (which will not be covered in this report) is that is can be steered in elevation as well as in azimuth. All simulations in this report will be in the azimuth plane (the plane of the array) at $\theta = 90°$.

Array Weighting

By operating on the virtual array manifold $\mathbf{b}(\mathbf{k})$ with a weighting vector $\mathbf{w}_{PM}^H$, the desired beam pattern can be created using the same weightings as for a ULA.

A special type of weighting used in the simulations of the UCA is the Villeneuve modification of the Dolph-Chebychev distribution. The Dolph-Chebychev distribution uses orthogonal Chebychev polynomials to produce a weighting vector that is optimal in the sense that it gives the minimum 3-dB bandwidth for a specific sidelobe level. This weighting technique can be used to lower the sidelobes to a desired level. It does, however, produce a constant sidelobe level. In some applications, decaying sidelobes are preferred. The Villeneuve modification introduces decaying sidelobes at a minimal increase of the 3-dB beamwidth by combining the Dolph-Chebychev weighting and the uniform weighting. For details of the weighting vector and a discussion of its optimality, see Van Trees [6].

Element spacing

The effects of the spacing of the elements in the UCA are a bit more complicated than for the ULA. Although theory implies that an element spacing of $d < \lambda/2$ is required to avoid grating lobes in the beampattern, when performing the simulations, other undesired effects appeared in the beampattern of the UCA for values of d close to, but less than $\lambda/2$. This will be covered in the simulations section.

2.5 Simulations of the UCA

All simulations in this section were made in MATLAB on a 32 element UCA set to receive an incoming plane wave with frequency $500kHz$ and a propagation velocity of $4660m/s$, the typical values of an AE source in copper.

2.5.1 Effects of Element Spacing

When the element spacing d is close to, but less than $\lambda/2$, the beampattern of the UCA does not match the theoretically calculated beampattern. This can be seen in Fig 2.8, in which the simulated beampatterns are plotted together with the theoretical ones, for different radius coefficients r_c, $(d = r_c \cdot \lambda/2)$. It is seen that the simulated beampattern differ more from the theoretical pattern for values of d closer to $\lambda/2$. While main lobe seems almost unaffected by this, the sidelobe behavior is distorted.

For values of r_c close to 1, the sidelobe level is not even decaying, one of the prime benefits of the Villeneuve distribution. This strange and undesired behavior of the beampattern required further analysis. It was discovered that for values of r_c close to 1, the beamforming matrix $\mathbf{B}_{PM}^{H}$ does not synthesize a *real-valued* beamspace manifold. This was in contrast to the literature [8], in which it is stated that the synthesized virtual beamspace manifold $\mathbf{b}(\mathbf{k})$ is real-valued.

Exactly why this is the case has not been covered in any available literature, but it might have something to do with the residual terms in the phase mode representation that are assumed to be negligible, at least for an element spacing d a bit smaller than $\lambda/2$. For r_c close to 1, the contributions of the residual modes may be significant. This is not proven, but it is consistent with the simulation shown in Fig. 2.8, where the simulated values seem to converge to the theoretical results when r_c is decreasing.

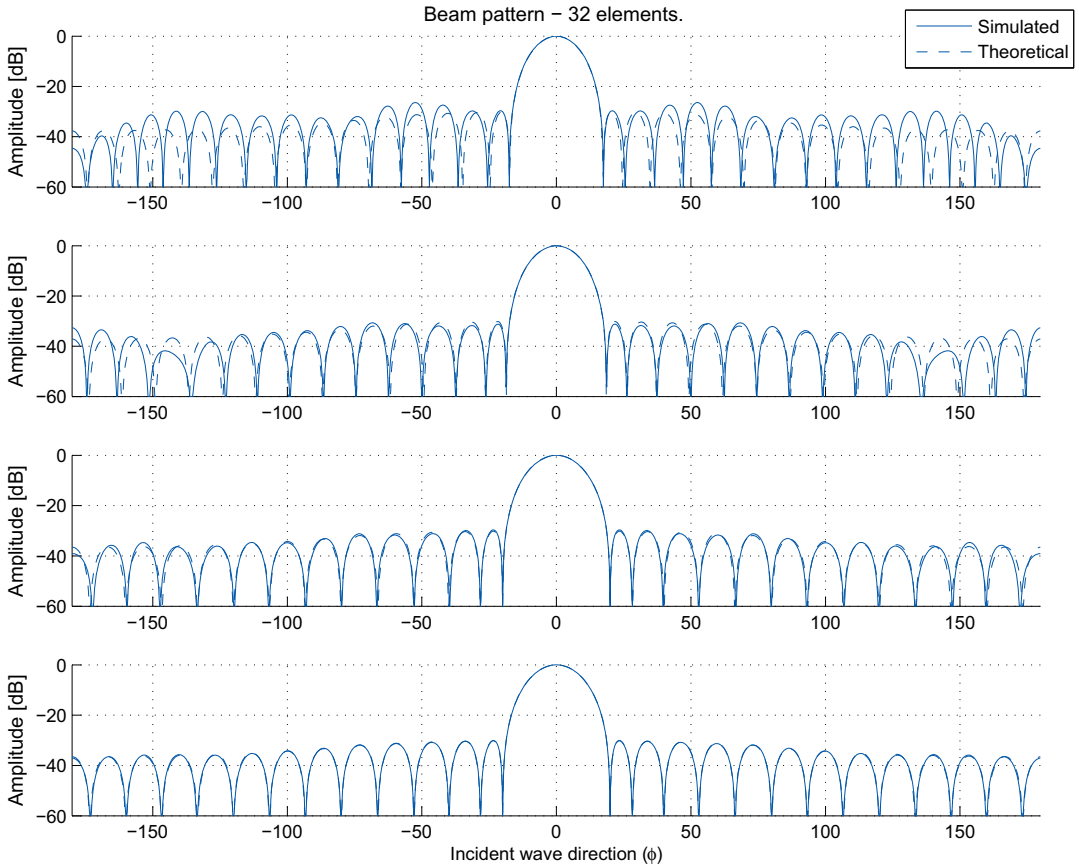

Figure 2.8: Simulated and theroretical beampatterns for a 32 element UCA with r_c of $1, 0.95, 0.90$ and 0.85, steered to $\phi_s = 0°$, using a -30dB sidelobe level Villeneuve weighting.

As a result of this finding, some tests were run to find a good value of r_c. It can be seen in Fig. 2.8 that a smaller r_c gives a good sidelobe behavior at the cost of a slightly decreased resolution. The 3-dB beamwidths for the beam patterns in Fig. 2.8 are, respectively, $13.2°, 13.9°, 15.0°$ and $15.0°$. The fact that the 3-dB beamwidths for $r_c = 0.90$ and $r_c = 0.85$ are equal is interesting. Since the simulated beampatterns for these values of r_c better match the theoretical beampatterns than for higher values of r_c, a good value of r_c could be in this range. For the rest of the simulations, $r_c = 0.875$ was used.

2.5.2 Effects of Array Steering

Simulations were performed to verify whether the UCA's beampattern in the azimuth plane for different steering angles remains essentially unchanged. Fig. 2.9 shows the results of the simulation of the UCA beamformer with a -30dB Villeneuve weighting for steering angles of $0°, 50°, 100°$ and $150°$. The 3-dB beamwidths are almost $15.0°$ in all cases. The small variations that occur are due to the resolution of the ϕ axis, as it is discrete.

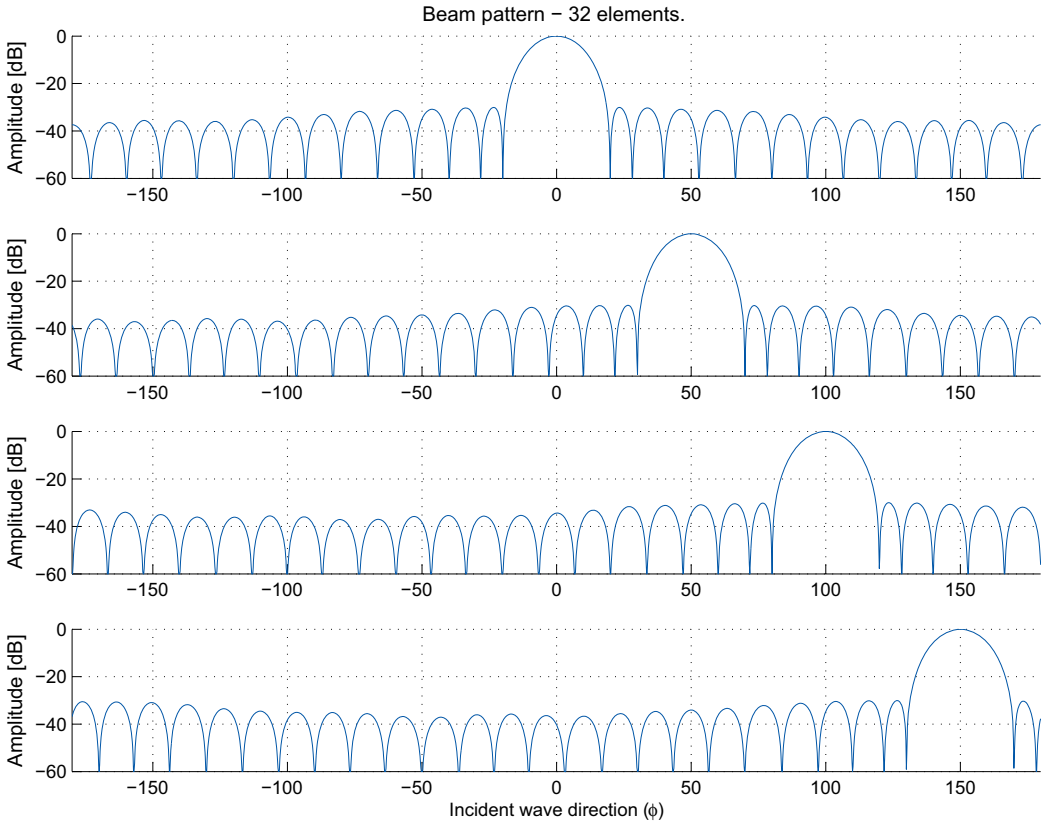

Figure 2.9: Beam patters for a 32 element UCA steered to $0°, 50°, 100°$ and $150°$, using a -30dB Villeneuve weighting, with $r_c = 0.875$.

2.5.3 Effects of Different Weighting Windows

Fig. 2.10 shows the azimuthal beampattern of a UCA obtained with a phase mode excitation beamformer using different weighting functions: uniform, Kaiser, Hamming and Blackman. These functions are well-defined standard windows with known properties. The sidelobe levels for those weightings are, respectively: $-13dB$ for the uniform weighting, $-41dB$ for the Hamming weighting, and $-57dB$ for the Blackman window. The Kaiser window function is defined using a real number β that defines the shape of the window. Here, $\beta = 2$ has been used, which gives a sidelobe level of $-19dB$. Increasing the number gives lower sidelobe levels and a wider main lobe.

The 3-dB beamwidths for the above windows are, respectively, $11.7°, 13.5°, 17.8°$ and $22.9°$. The 3-dB beamwidths are not only affected by the weighting function used, they also depend on the number of elements if the UCA, as well as its radius.

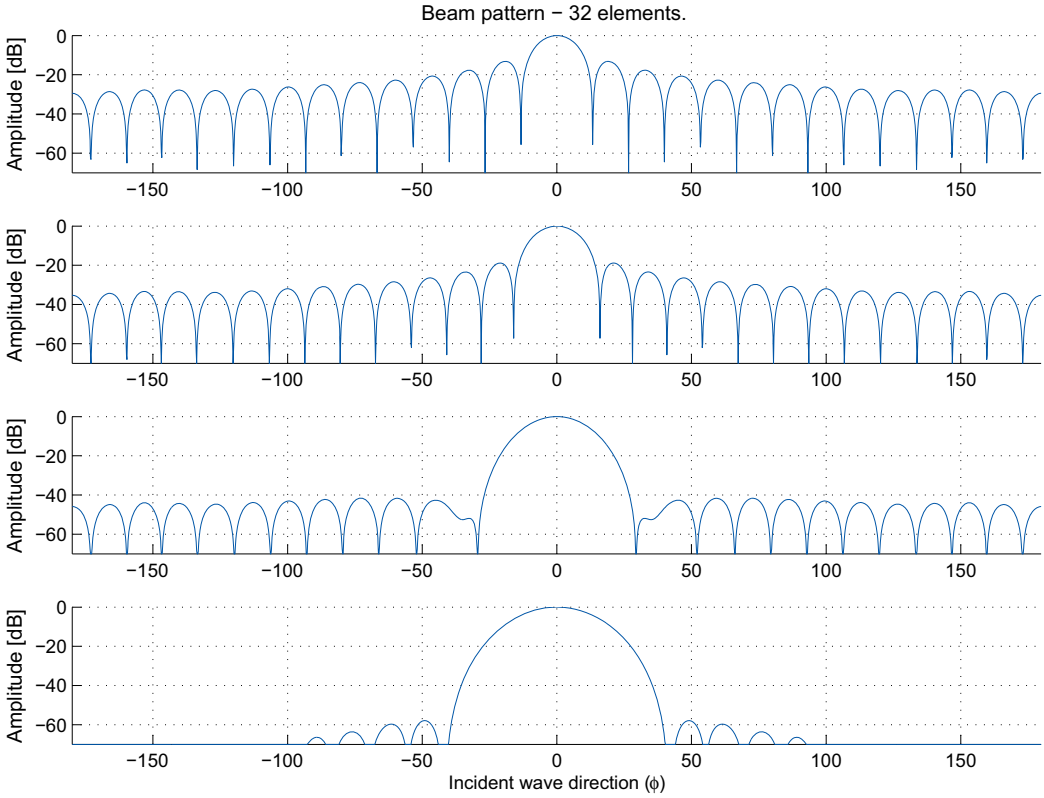

Figure 2.10: Beampatterns for a 32 element UCA steered to 0°, using: (a) uniform window; (b) Kaiser window; (c) Hamming window; (d) Blackman window.

Using the Villeneuve modification of the Dolph-Chebychev distribution, it is possible to minimize the 3-dB beamwidth for a desired sidelobe level. The results obtained using this weighting function, given sidelobe levels of $-20dB, -30dB, -40dB$ and $-50dB$, are presented Fig. 2.11. The 3-dB beamwidths for these weightings are, respectively, $12.8°, 14.9°, 16.7°$ and $18.2°$.

Because the sidelobe level can be chosen as desired, the Villeneuve distribution weighting can be compared with the types of weighting presented in Fig. 2.10. Using a Villeneuve distribution with sidelobe level equal to the standard weighting windows, it is possible to see how much performance that can be gained. Performance of the Villeneuve weighting is compared to that of standard windows in Table 2.1. There is no simple expression for how much the resolution can be improved by using the Villeneuve distribution but it is clear that the Villeneuve weighting outperforms the standard window in terms of resolution given sidelobe level.

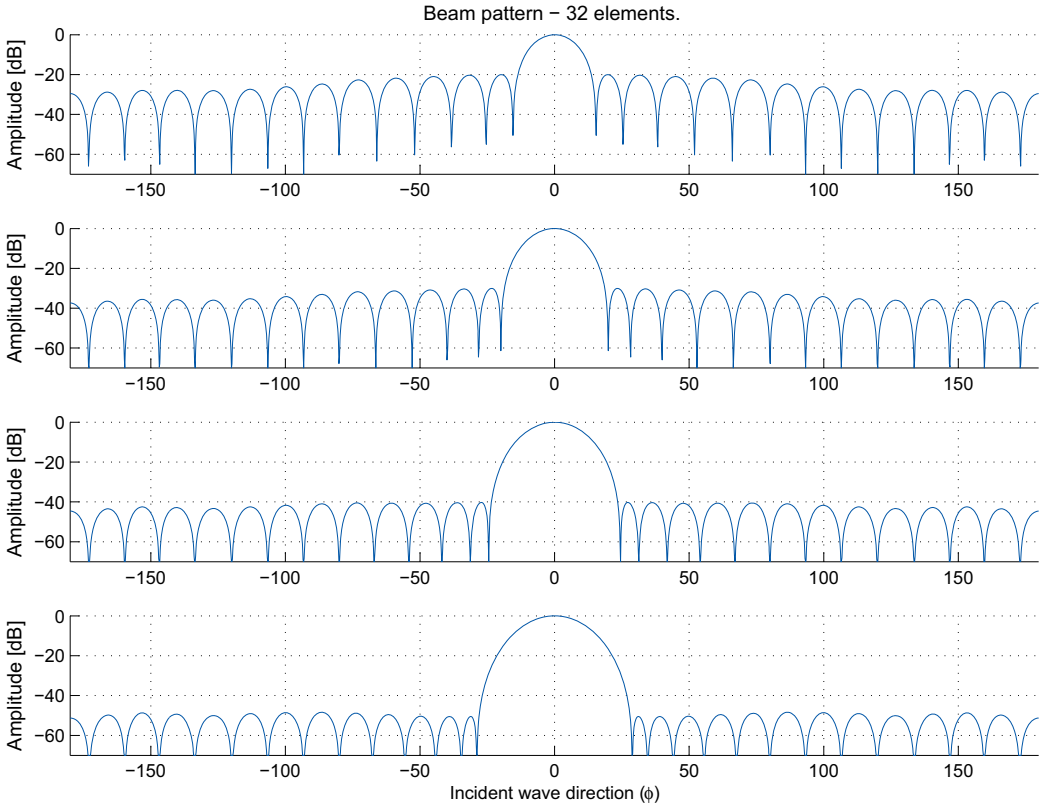

Figure 2.11: Beampatterns for a 32 element UCA steered to 0°, using a Villeneuve weighting function with sidelobe levels of $-20dB, -30dB, -40dB$ and $-50dB$, respectively.

Sidelobe level	Standard	Villeneuve	Resolution improvement
$-13dB$ (Uniform)	11.7°	11.0°	$\sim 6\%$
$-19dB$ (Kaiser)	13.5°	12.4°	$\sim 9\%$
$-41dB$ (Hamming)	17.8°	16.7°	$\sim 7\%$
$-57dB$ (Blackman)	22.9°	18.9°	$\sim 21\%$

Table 2.1: Comparisons of the standard weighting windows and the Villeneuve distribution.

2.5.4 UCA and Pulse Signals

Up to this point, all theory and simulations have assumed an input in the form of a continuous wave with a single frequency of $500kHz$. The next step is to test the behavior of the UCA for a broadband pulse, which includes several superimposed frequencies. The standard way is to assume a pulse in the form of a continuous sine wave with a frequency of $500kHz$ modulated by a Gaussian window. This is a reasonable approximation of a signal generated by a AE sensor receiving a single AE event. The discrete-time pulse consists of 512 samples obtained at a sample rate of $1.25MHz$ ($2.5 \cdot 500kHz$ to avoid aliasing effects). The oversampling is a precaution for the case when the pulse includes a higher frequency components than $500kHz$. The pulse and its frequency spectrum are shown in Fig. 2.12. As seen in the figure, the frequency spectrum is centered at $\pm 500kHz$, and the pulse consists mostly of frequencies around this frequency. The

exact look of the frequency plot can be altered by changing the width of the Gaussian window.

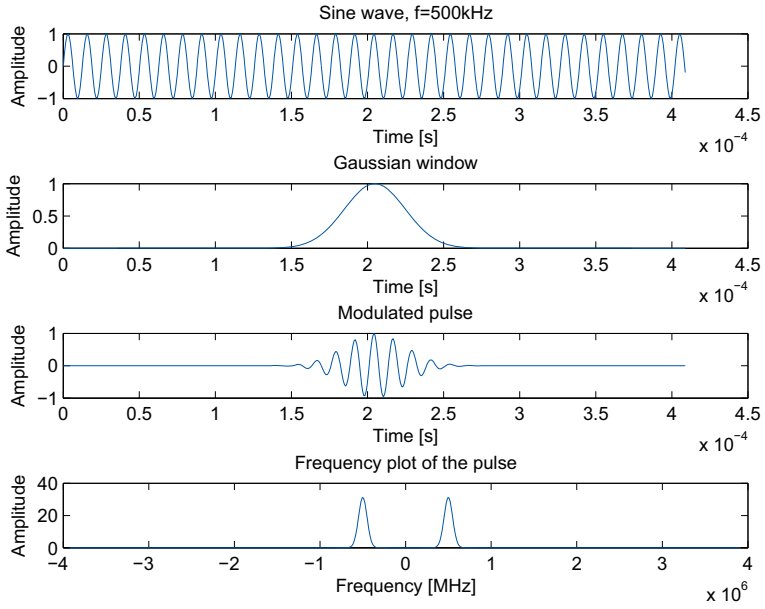

Figure 2.12: Defining the pulse. (a) Sine wave with $f = 500kHz$; (b) normalized Gaussian window; (c) the modulated pulse; (d) amplitude frequency spectrum of the pulse.

2.5.5 Frequency Dependency of the UCA

Let us start the UCA analysis for impulse input with investigating the effects of the input signal in the form of continuous waveform with varying frequency.

Below, we will present simulations performed using single continuous waves with frequencies ranging from $250kHz$ to $750kHz$ as inputs to the UCA. The UCA and the corresponding beamforming matrices $\mathbf{B}_{PM}^{H}, \mathbf{J}_{\zeta}, \mathbf{C}_{j}$ and $\mathbf{V}^{H}$ defined in section 2.4.1 were defined for the center frequency of $500kHz$. The UCA was then simulated using the above frequency range to see how the beampattern of the UCA depends on the frequency of the incoming signal. This was done by changing the array manifold vector $\mathbf{v_k}(\mathbf{k})$ using different frequencies in the above frequency range. It would be desirable to get a frequency-invariant beampattern, i.e., that the UCA would produce the same beampattern for all frequencies. As was shown in section 2.4.1, this is not possible, since for the high frequencies, the spacing d of the elements will be significantly larger than $\lambda/2$ and aliasing effects will be present in the beampattern.

Fig. 2.13 shows the results of this simulation. For each frequency, the UCA beampattern was calculated and plotted in an aggregated intensity plot. While it can be seen that for an input frequency of $500kHz$, the beampattern of the UCA has the desired main- and sidelobe behaviour, it fails to produce the desired beam pattern for any other frequency. These results illustrate the fact that the fixed beamforming matrices used with the UCA cannot handle signals that consist of several frequencies.

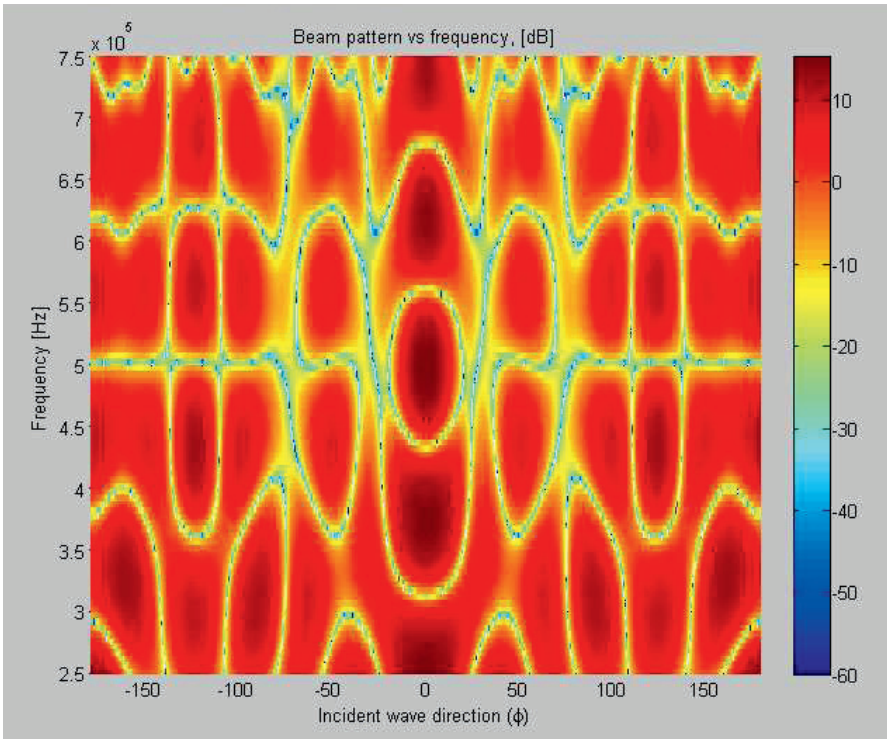

Figure 2.13: Dependency of the beampatterns on incoming wave frequency. UCA set to receive signals at $f = 500kHz$.

Literature studies on the subject of frequency invariant beamformers for UCA revealed that it was possible to achieve a virtually frequency invariant result by modifying part of the beamforming matrices with respect to the frequency [9], [10]. By letting the elements in the matrix $\mathbf{J}_\zeta$ depend on the input frequency, the frequency dependency in each phase mode m can be compensated [9]. The disadvantage to this is that the beamforming matrices have to be recalculated for every single frequency, leading to a longer computation time. This approach is illustrated in Fig. 2.14, which shows a substantial improvement over the result in Fig. 2.13. Using the matrix $\mathbf{J}_\zeta$ as a frequency dependent filter, the UCA produces the desired beampatterns for low frequencies, but as the frequency increases, some aliasing effects occur and degrade the beampattern. Reducing the radius of the array will shift these effects to higher frequencies, but as noted in section 2.5, Fig 2.8, the 3-dB beamwidth will increase as a result. The factor r_c governing the radius has been set to 0.875 in all simulations in this section.

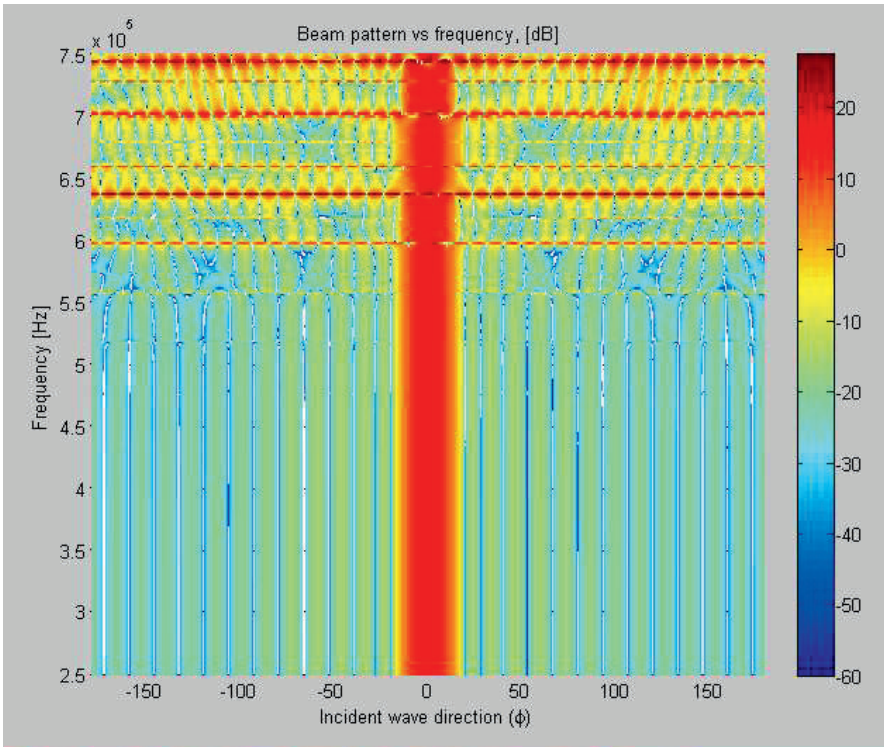

Figure 2.14: Dependency of the beampatterns on incoming wave frequency using a frequency compensating filter. UCA set to receive signals at $f = 500kHz$.

These above results are very promising since they indicate that the UCA can be used on pulse signals if the frequency dependent matrix $\mathbf{J}_\zeta$ is applied in the beamformer.

Some undesired effects may occur if a frequency component is located precisely at such a frequency that accordingly to Fig. 2.14 will give rise to a beampattern that has no angular selectivity. Examples of such frequencies in Fig. 2.14 are $596kHz, 636kHz$ and $700kHz$. Some additional inspections of how the beampatterns look near these frequencies were performed.

In Fig. 2.15 the beampatterns of the UCA for frequencies in the range of $595kHz$ to $598kHz$ with a resolution of $0.05kHz$ have been plotted. It can be seen that for a narrow frequency band around $596kHz$, the UCA loses its angular selectivity. What is also negative is that a signal originating from an arbitrary angle at this exact frequency will be significantly stronger than a signal originating from the current steering angle with a different frequency. While not shown here, the beampatterns around the other frequencies mentioned in the above paragraph have the same appearance. This could cause problems when working with a pulse signal. Fortunately, the frequency band where this occurs is comparatively narrow, and the effects of this may not be as severe as it may appear. As with the more general aliasing effects that occur for higher frequencies, these effects can also be shifted to higher frequencies by lowering the r_c coefficient.

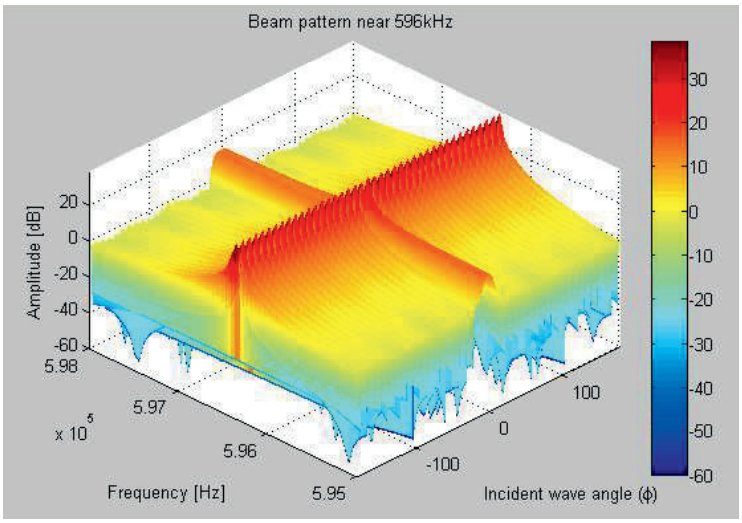

Figure 2.15: Detailed look on the beampatterns of the UCA near $596kHz$.

With these results at hand, the UCA could now be simulated using a pulse as the incoming signal.

UCA Response to an Incoming Pulse

For the input pulse that was defined above the spectral information is concentrated in the relatively narrow frequency band around $500kHz$ (see Fig. 2.12).

To simulate the UCA response to this pulse, we took the following approach, based on the method and results of section 2.5.5. Using the information in the amplitude plot, a separate array manifold vector $\mathbf{v_k}(\mathbf{k})$ was constructed for each frequency present in the pulse and scaled according to its relative amplitude. Also, for each frequency, the matrix $\mathbf{J}_\zeta$ was updated, the beamforming matrices were recalculated and the responses from the array for each frequency were calculated. The result at this point was another amplitude plot of the frequency spectrum, which shows how much the UCA amplified or damped the frequencies. This spectrum was then inverse Fourier transformed back into time domain to see how the time-signal was altered by the UCA.

Fig. 2.16 shows the result of a simulation of pulse wave incoming from the azimuth $\phi = 0°$ to a 32 element UCA steered to $\phi_s = 0°$ using a $-30dB$ Villeneuve weighting. The AMP value in the figure is a number that shows the relative magnitude of the output. It is calculated using a Hilbert transform on the time signal output. This value is used to relate amplitudes of pulses from different incoming angles to each other.

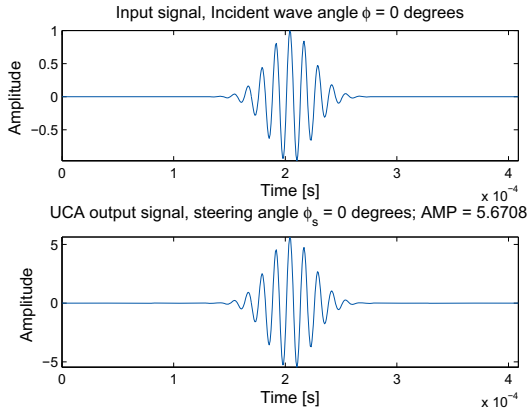

Figure 2.16: UCA simulated for an incoming pulse.

From Fig 2.16, it is clear that the UCA can reproduce the input pulse signal, so the effects described in Fig 2.15 appear to not seriously hamper the UCA performance on pulse signals, at least not for sufficiently low frequencies. Since the signal in Fig 2.16 was set to coincide with the steering angle of the array, it would be expected that a signal originating from other azimuth angles would have a lower relative amplitude. In Fig 2.17, the same UCA were simulated, using the angles of $0°, 8°, 20°$ and $23°$, respectively. It can be seen that the amplitudes of the output are lower for the angles not coinciding with the steering angle. Note that the angles used in the present simulation correspond to the characteristic points of the beampattern shown in Fig. 2.11 (second plot), i.e., the mainlobe maximum ($0°$), the -3dB angle ($8°$), the first minimum ($20°$) and maximum of the first sidelobe ($23°$). If the normalized relative amplitudes are converted to the decibel scale, the relative amplitudes are approximately $0dB, -3.4dB, -49dB$ and $-30dB$, respectively. These values correspond well to the ones expected from looking at Fig. 2.11.

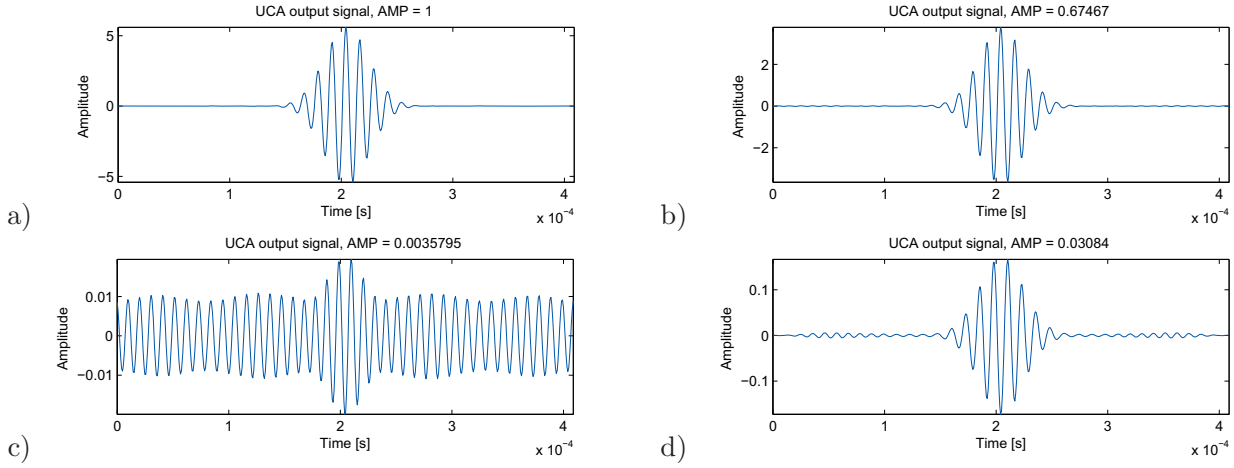

Figure 2.17: UCA simulated for an incoming pulse with different incoming angles ϕ. (a) $\phi = 0°$; (b) $\phi = 8°$; (c) $\phi = 20°$; (d) $\phi = 23°$;

The output signal in plot (c), corresponding to the first minimum of approximately $-50dB$ does not resemble the input signal at all. This is because the array is designed to attenuate all signals from this direction so that they have much lower level than the ones coming from the steering angle. The exact appearance of the UCA output from this angle is not important as long as it is sufficiently attenuated. It can also be discerned that shape of the output signal

compared to the original signal degrades the more the signal is attenuated. Small ripples are present in the output signal in plot (b) and even more so in plot (d).

The following plots show simulations illustrating how the UCA responds to a pulse when the center frequency is not exactly $500kHz$. Such pulses are easily defined using the desired center frequency as the frequency in the sine wave from Fig 2.12. From Fig. 2.14, it can be expected that the UCA will perform better on lower frequency pulses than on higher frequency pulses, where aliasing effects will occur. Fig. 2.18 shows the result of this simulation.

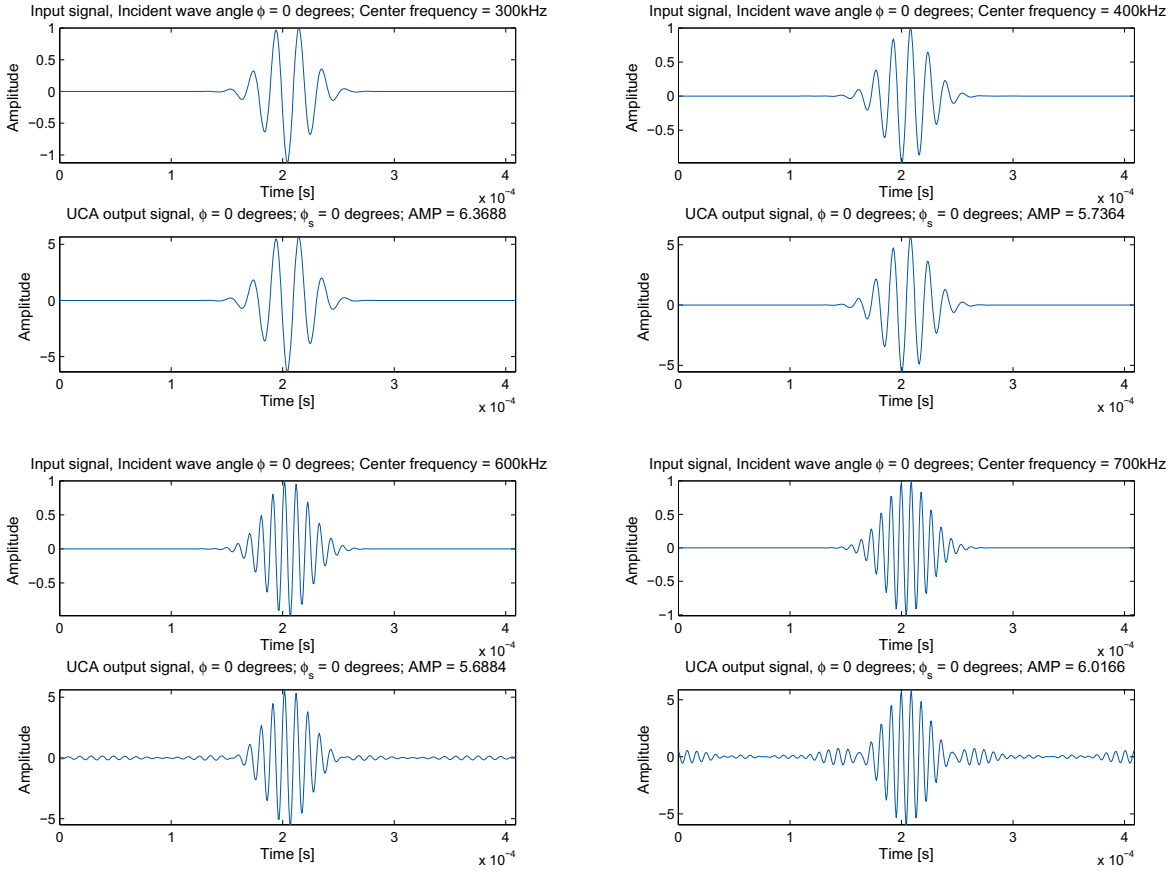

Figure 2.18: UCA simulated for an incoming pulse with different center frequencies.
(a) $f_c = 300kHz$; (b) $f_c = 400kHz$; (c) $f_c = 600kHz$; (d) $f_c = 700kHz$;

The results indicate that the UCA can handle pulses in a wide range of frequencies without major problems and produce an output that is somewhat similar to the input for higher frequency pulses and very similar for lower frequency pulses. However, a complete beampattern had to be computed for each pulse to determine the UCA performance.

Steering

As described in section 2.4.1, an important advantage of the UCA is that the beampattern is essentially unchanged for all steering directions in azimuth. This means that the shape and relative amplitude of the pulse should be virtually independent of the steering angle. Also, due to the symmetry of the UCA, a signal originating from any azimuth coinciding with an angle where an element of the array is located should produce the same output as long as the array

is steered to this particular angle and the input pulse is constant. In the example in Fig. 2.17, one of the array elements is located at $\phi_0 = 0°$. In a 32 element UCA, the angular spacing of the elements is 11.25°, so if the steering angle and the angle of the incoming pulse are both set to any angle $k \cdot 11.25°$, where k is an integer, the output of the UCA should exactly match the output in the (a) plot in Fig. 2.17. A plot showing the results of this simulation is in Fig. 2.19, where the angles of interest have been set to $10 \cdot 11.25°$. The AMP value of the pulse is the same as in Fig. 2.17(a) and it was proven in MATLAB that the shape of the pulses are identical.

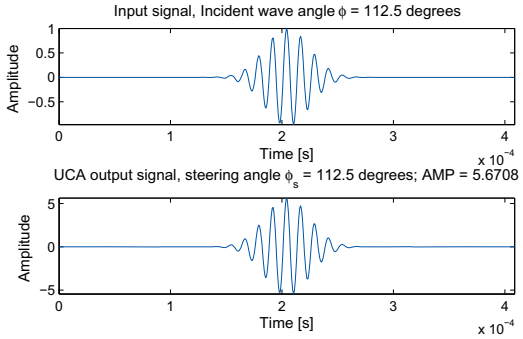

Figure 2.19: UCA simulated for an incoming pulse. $\phi, \phi_s = 112.5°$, set to coincide with the angle of an element in the UCA.

Using $10 \cdot 11.25°$ as the steering angle, and with the symmetry properties of the UCA, incoming pulses from $120.5°, 132.5°$ and $133.5°$ should all produce exactly the same outputs as the remaining plots in Fig. 2.17, which was confirmed by the simulations.

Also it has been tested how the beamformer output changes for the angles ϕ, ϕ_s set to the same value, which does not coincide with any element angle. Using a signal sampled at 512 points, the maximum relative change of the amplitude of the signal was at most 0.7%, which occurs for angles ϕ, ϕ_s exactly between the two element angles and hopefully is insignificant. The exact change in amplitude depends on the shape of and the number of samples in the pulse.

Beampatterns

As mentioned previously, by inspecting the relative amplitudes of signals originating from $\phi \in [-\pi, \pi]$, a beampattern of the UCA responding to the pulse in Fig 2.12 can be computed and compared to the beampattern of the UCA calculated for a continuous wave with a single frequency of $500kHz$. In Fig. 2.20, the beampatterns for a 32 element UCA using a single frequency input signal and a pulse input signal have been plotted for comparison. The values for the pulse signals presented in Fig 2.17 are marked with x-es in Fig 2.20.

Comparison of both plots in Fig 2.20 reveals that while the beampatterns are not identical, they still have the same mainlobe width and a similar sidelobe behavior. It should be noted that the plots have different angular resolutions, in the top plot it is 0.18° while for the bottom plot it is 1°. This partially explains why the nulls in the bottom plot with an incoming pulse signal are not as deep as for the single frequency wave. Another factor is that since the bottom plot essentially is a combination of many beampatterns corresponding to different frequencies, some smearing effects are expected. If the signal is sampled at a higher sample rate, it will contain a higher number of frequencies and the smearing effects will be more evident.

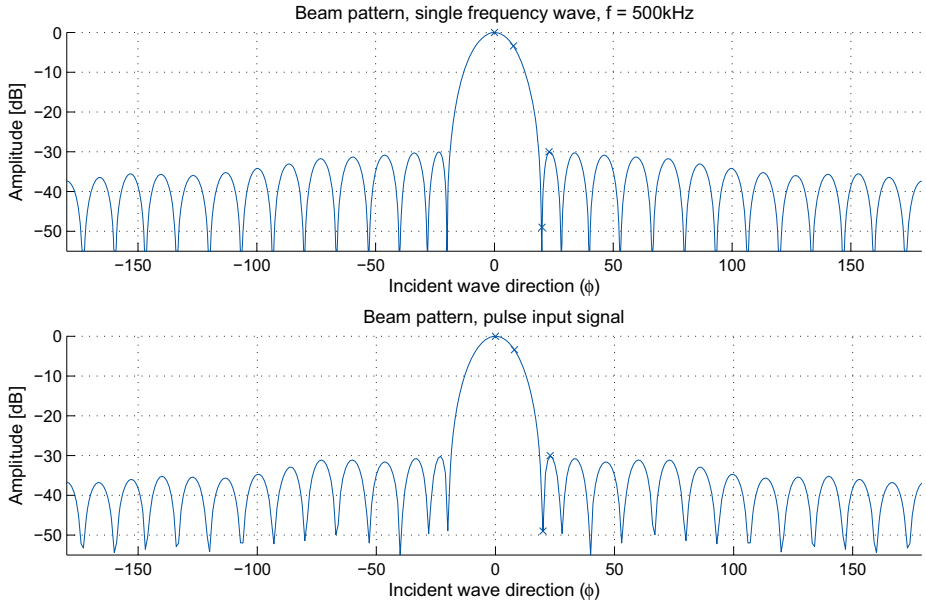

Figure 2.20: Beampattern of the UCA simulated for a $500kHz$ continuous wave (upper part), and for the pulse shown in Fig. 2.12 (lower part).

Fig. 2.21 shows the UCA beampatterns obtained for the pulse input signal for four other types of weighting windows. They can be compared to the respective beampatterns for a continuous wave with a single frequency, shown in Fig. 2.10. Comparison shows that the UCA has almost the same performance for the pulse input as for the single frequency case.

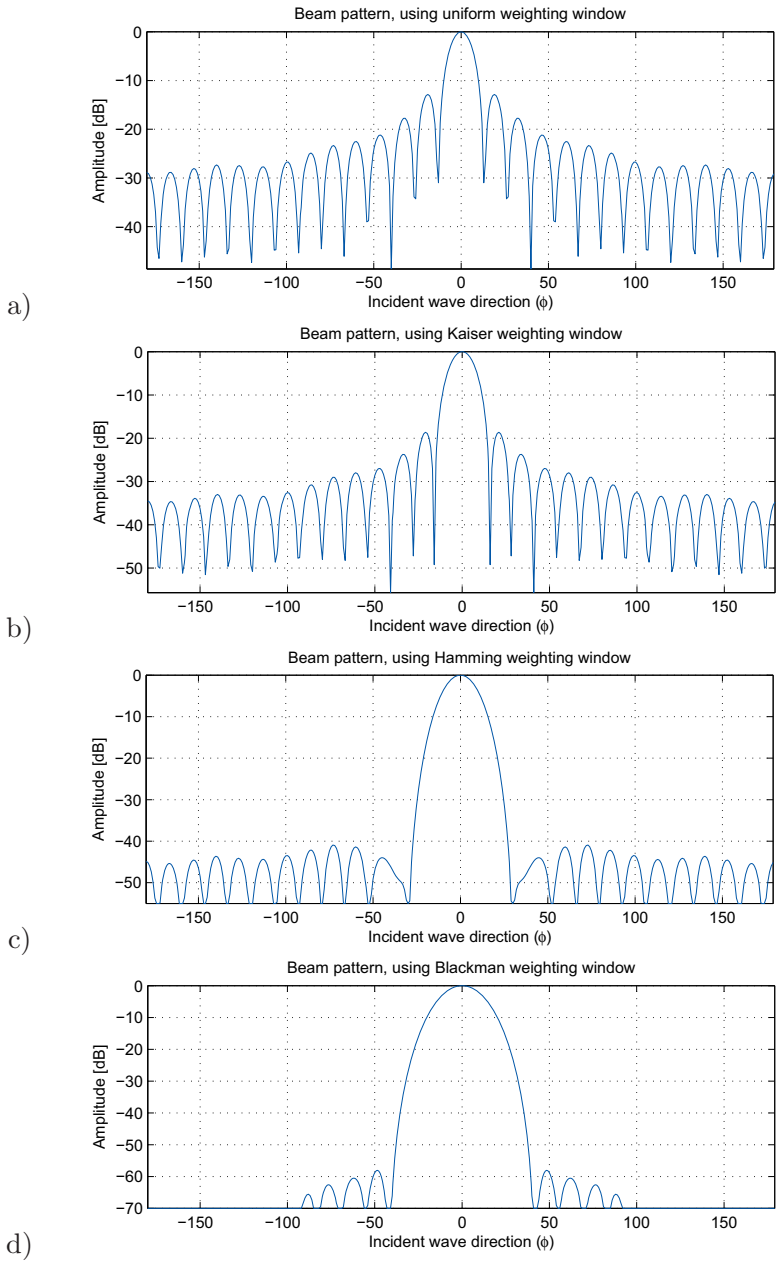

Figure 2.21: Beampatterns for UCA simulated for an incoming pulse using different weighting windows. (a) uniform window; (b) Kaiser window; (c) Hamming window; (d) Blackman window.

The results presented in previous section indicate that the UCA can performs well for pulses in a wide range of frequencies. Complete beampatterns were computed for each pulse shown in Fig. 2.18 to determine the UCA performance. The beampatterns are shown in Fig. 2.22, from which it is seen that the beampatterns for low frequency pulses are almost identical to the one for the $500kHz$ single frequency wave shown in Fig. 2.20, while the beampatterns for high frequency pulses have degraded somewhat. This means that the UCA can be used to detect signals within a wide frequency range with fairly good results.

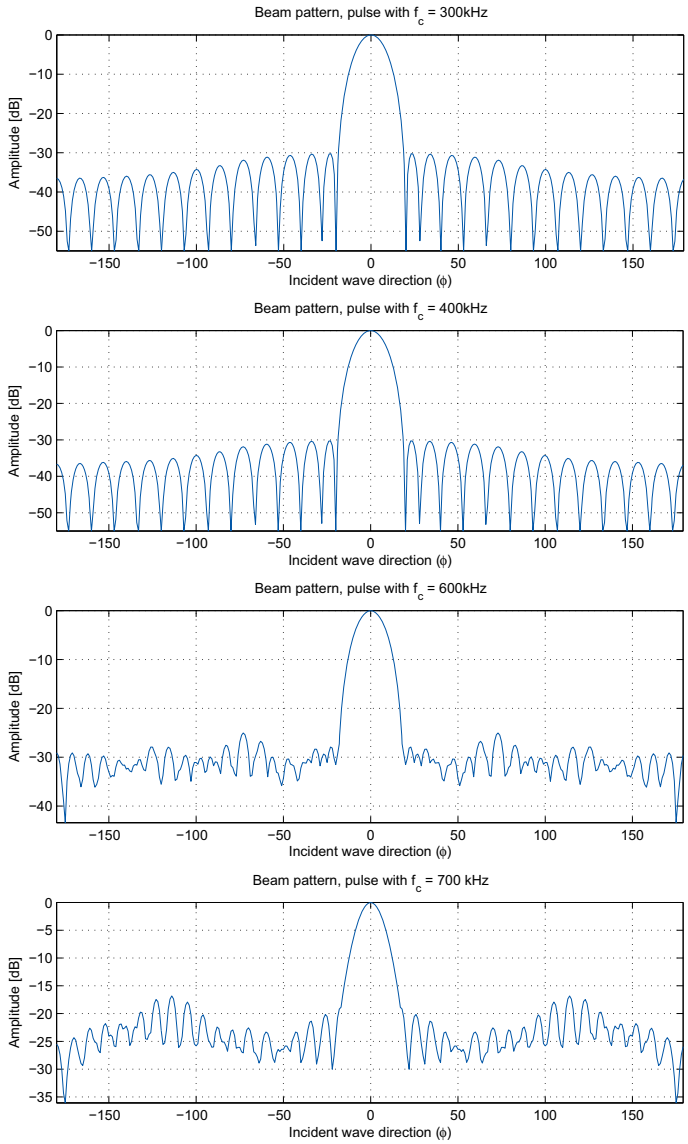

Figure 2.22: Beampatterns for the UCA using an incoming pulse with different center frequencies. (a) $f_c = 300kHz$; (b) $f_c = 400kHz$; (c) $f_c = 600kHz$; (d) $f_c = 700kHz$;

Summarizing, it has been proven that the UCA is able to enhance the strength of a pulse waves coming from the steering directions while attenuating pulses from other directions, at least for ideal, noise-free signals.

2.5.6 Performance Evaluation for Noisy Signals

As a last step in simulating the UCA, zero-mean white Gaussian noise was added to the input pulse to see how this would affect the performance. Fig. 2.23 shows two pulses with relative added noise amplitudes of $N_0 = 0.1$ and $N_0 = 0.3$, which results in the signal to noise ratios of 20dB and 10dB, respectively. The corresponding amplitude frequency spectra of the two pulses are also plotted for comparison.

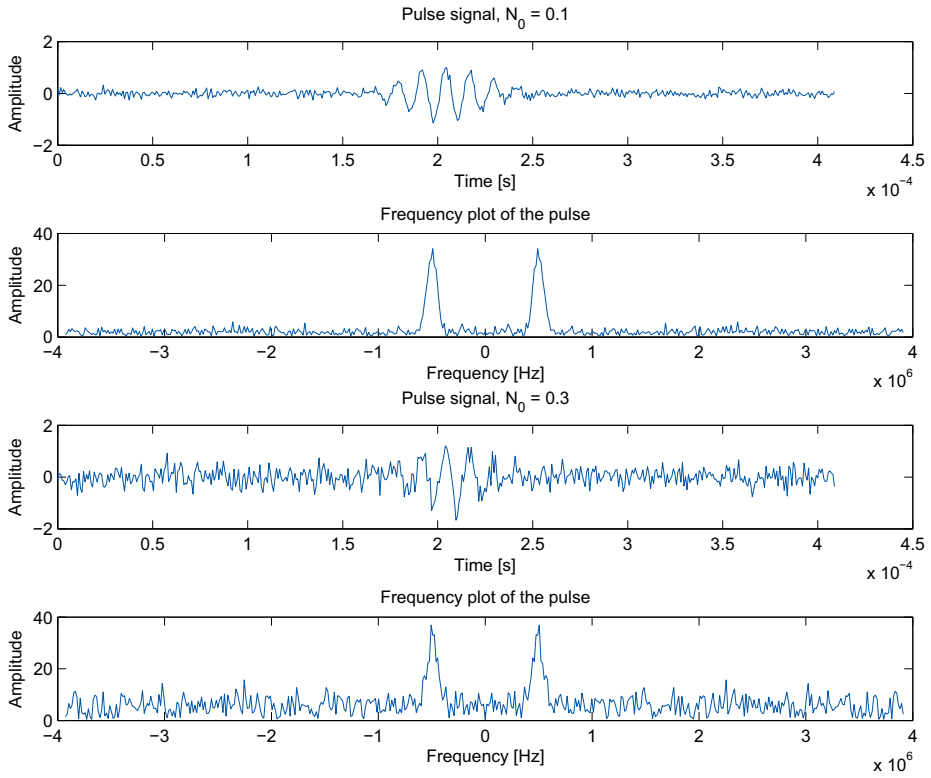

Figure 2.23: Noisy pulse input signals and their corresponding amplitude frequency spectrum. (a,b) $N_0 = 0.1$; (c,d) $N_0 = 0.3$. The pulse has unit amplitude.

The distorting Gaussian noise is present at all frequencies, which means that the pulses are not narrowband signals centered at $500kHz$ any longer. When a noisy signal appears at the UCA's input its output is clearly affected, which is shown in Fig. 2.24. As is clearly seen, the UCA completely fails to recognize the signal, as the output from it seems to be a high-amplitude noise. It is not shown here, but the UCA is so sensitive that its performance is seriously impared even for the noise level N_0 as small as 0.001.

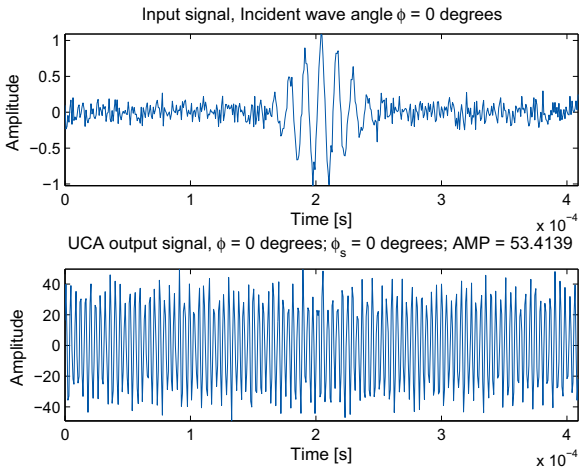

Figure 2.24: UCA simulated for an incoming unit pulse with additive noise amplitude $N_0 = 0.1$.

This rather unexpected and disappointing result had to be investigated more closely. As explained previously in this section, the beamforming matrices in our UCA beamformer are updated for every frequency present in the pulse. The result of this is an amplitude frequency spectrum, which shows how much the UCA reinforces or attenuates different frequencies. This spectrum is then inverse Fourier transformed into time-domain to reproduce the time-domain output of the UCA. The UCA's output spectrum for the signal shown above is in Fig. 2.25.

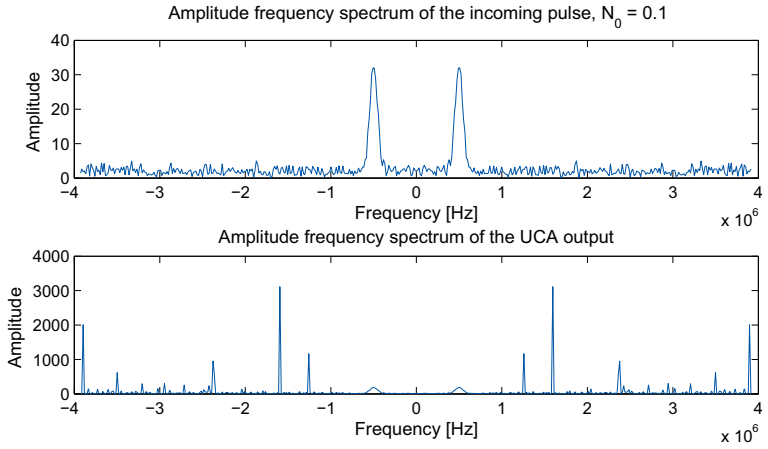

Figure 2.25: Amplitude frequency spectrums of the input and output signals shown in Fig. 2.24.

From the amplitude spectrum it can be seen that seemingly random (high) frequencies are reinforced to the point that the frequencies containing information about the input pulse are proportionally insignificant, causing the output to be undesired, high-amplitude, high-frequency noise shown in Fig. 2.24. Because the phase-mode beamformer MATLAB script works with one frequency at a time, the beamforming matrices could be evaluated for each specific frequency to identify the source of problems. It was found that the frequency dependent filter, $\mathbf{J}_\zeta$, gives rise to the problem. The Bessel functions evaluated in $\mathbf{J}_\zeta$ look roughly like oscillating sine or cosine functions, decaying for higher arguments. Therefore, since the matrix $\mathbf{J}_\zeta$ appears in the denominator, the output frequency would be significantly amplified whenever a term in $\mathbf{J}_\zeta$ had an argument that resulted in a value close to zero.

A simple regularization method, commonly used in inverse filtering was proposed as a solution to this problem. By adding a small, dynamic term to the denominator it is possible to avoid that the denominator is too close to zero. In this way the very strong amplification of the high frequencies is limited, but at the price of some degradation of the UCA performance. Using this modification, the diagonal elements of $\mathbf{J}_\zeta$ matrix now look like

$$J_k^{-1}(\zeta) = \frac{J_k(\zeta)}{J_k(\zeta)J_k^*(\zeta) + \alpha_J}. \tag{2.3}$$

Due to this modification, the term α_J added to those products $J_k(\zeta)J_k^*(\zeta)$ that are close to zero limits the value of $J_k^{-1}(\zeta)$.

The disadvantage is that all elements in the denominator will be slightly larger than before, and this will attenuate all frequencies, giving a weaker output than before. In practical situations α_J has to be found by trial and error. Too large values will attenuate all frequencies too hard, while too small values will not sufficiently limit the value of $J_k^{-1}(\zeta)$. Examples of the amplitude spectrums of the UCA output obtained for the considered case with different values of α_J are shown in Fig. 2.26. It can be seen that for α_J as small as 0.0001, the noise at the higher frequencies is more pronounced than for higher values of α_J. At the same time, however, while the noise level is reduced the amplitude of the frequencies of interest at frequency band $500kHz$ is also lower.

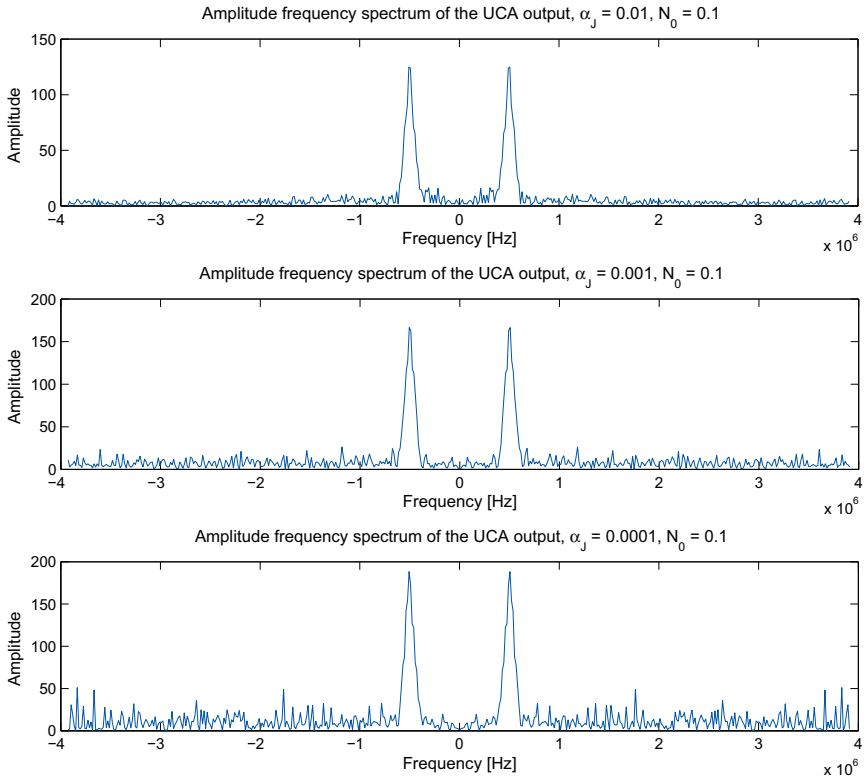

Figure 2.26: Amplitude spectrums of the UCA output for different values of α_J input input signals in the form of unit amplitude pulse with additive noise.

The time-domain output of the UCA for the respective values used in Fig. 2.26 is shown in Fig. 2.27. As expected, the output corresponding to $\alpha_J = 0.01$ shows the least noise, but also has the lowest relative amplitude, while the opposite holds for $\alpha_J = 0.0001$. In all cases, however, a substantial improvement over the output from Fig. 2.24 is apparent.

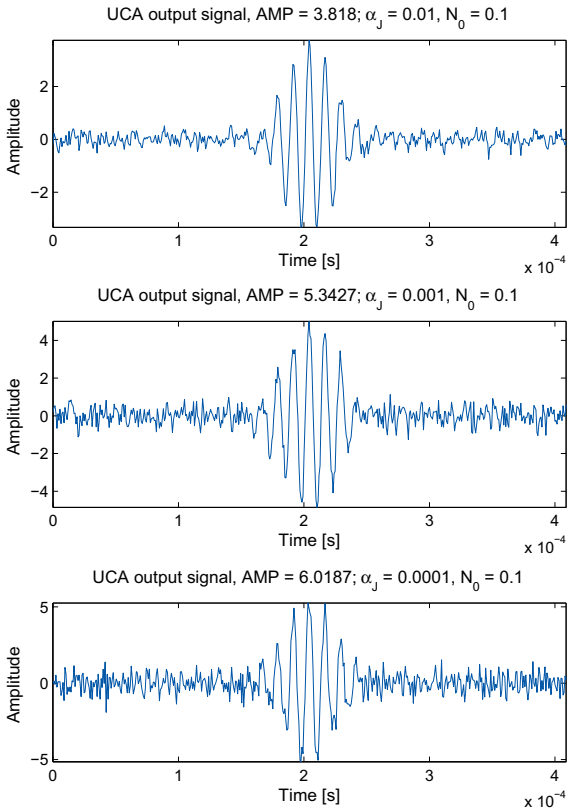

Figure 2.27: UCA output for different values of $\alpha_J$for the input signals in the form of unit amplitude pulse with additive $N_0 = 0.1$ noise.

With these results at hand, the entire beampattern of the UCA for noisy signals was simulated using various weighting windows, noise levels and values of α_J. Examples of the resulting beam patterns are presented in figures 2.28 to 2.33.

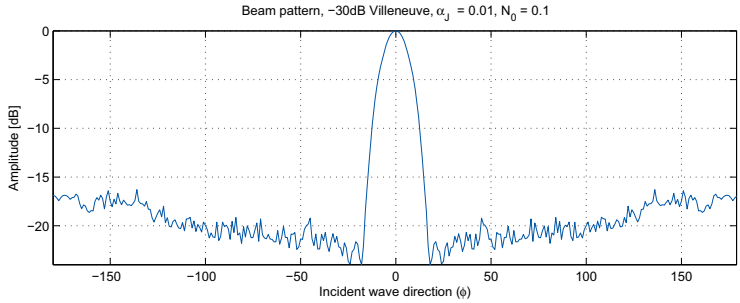

Figure 2.28: UCA Beampattern, using -30dB Villeneuve window, $\alpha_J = 0.01$, SNR $20dB$.

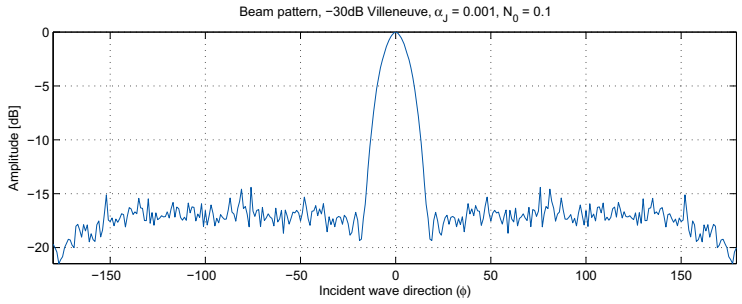

Figure 2.29: UCA Beampattern, using -30dB Villeneuve window, $\alpha_J = 0.001$, SNR $20dB$.

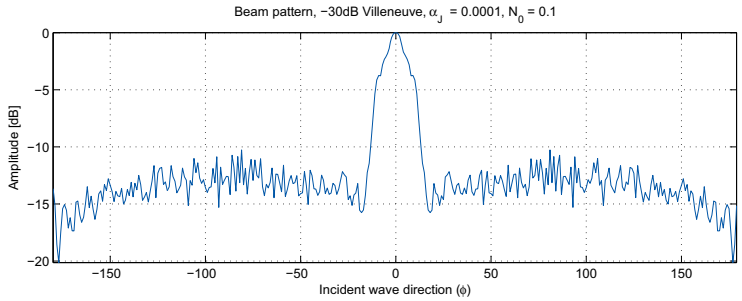

Figure 2.30: UCA Beampattern, using -30dB Villeneuve window, $\alpha_J = 0.0001$, SNR $20dB$.

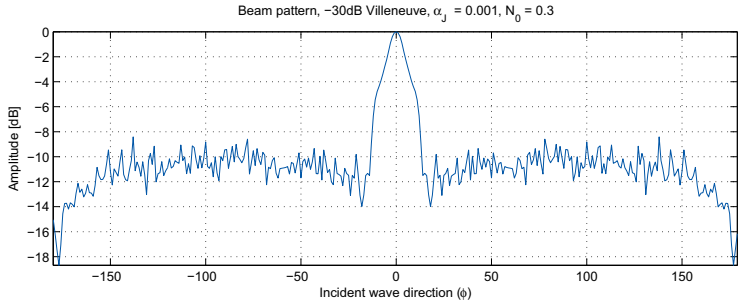

Figure 2.31: UCA Beampattern, using -30dB Villeneuve window, $\alpha_J = 0.001$, SNR $10dB$.

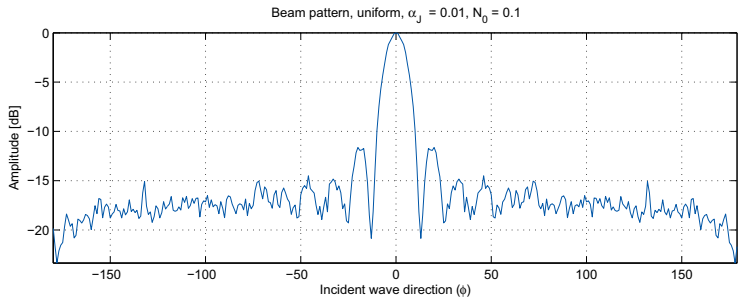

Figure 2.32: UCA Beampattern, using uniform window, $\alpha_J = 0.001$, SNR $20dB$.

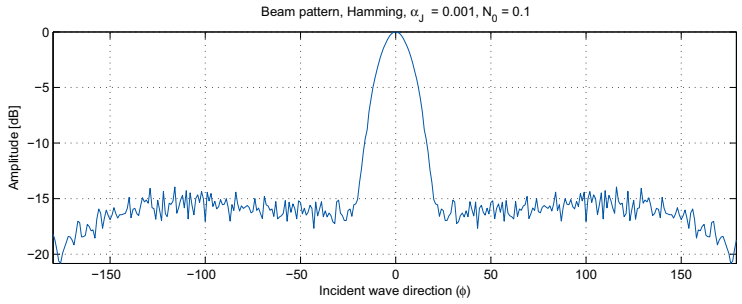

Figure 2.33: UCA Beampattern, using Hamming window, $\alpha_J = 0.001$, SNR $20dB$.

By inspection of the beampatterns, it is evident that the noise severely affects the UCA performance, especially regarding attenuating signals originating from angles other than the steering angle. Comparison of Fig 2.29 and Fig. 2.31, where only the SNR differs, it is evident that the UCA can not attenuate noisy signals as hard as for ideal noise-free signals. However, the simple regularization technique applied here, adding of a term in the denominator, reduces the most severe effects of the noise. By using more refined techniques and using some information about the signal it will be possible to enhance the UCA performance, although it is impossible to exactly determine the degree of improvement. This will not be covered in this report, where only the effect of noise was to be investigated.

2.6 Conclusions and Future Work

It has been shown that a UCA can achieve good angular selectivity using the phase mode excitation beamformer. The results of the simulations are satisfactory and show that using the Dolph-Chebychev distribution with the Villeneuve modifications, it is possible create a weighting function that achieves a desired beam pattern. The beampattern is optimal in the sense that for a given, desired sidelobe level, the width of the mainlobe is minimal. The UCA is furthermore shown to, despite some issues, perform well when operating on broadband signals, but its performance is hampered by noise. A simple technique for dealing with noise in the simulations was tested that gave positive result. More refined techniques are likely to produce even better results.

Future work includes, obviously, experiments. Simulations, while still an essential part, can only take the research so far. Experiments will have to be performed on a prototype UCA setup to investigate whether external sources give rise to further issues, and if they do, they will have to be dealt with. Also, more simulations may have to be done regarding the effects of noise, which was only briefly reviewed in this thesis. A final system must also be able to monitor the FSW process in real-time.

Based on the simulation results obtained up to date we are convinced that UCAs are a very promising tool for monitoring of the FSW process.

Bibliography

[1] W.M. Zeng, H.L. Wu, and J. Zhang. Effect of tool wear on microstructure, mechanical properties and acoustic emission of friction stir welded 6061 Al alloy. *Acta Metallurgica Sinica(English Letters)*, 19(1):9–19, 2006.

[2] Han-Ki Yoon, Yu-Sik Kong, Seon-Jin Kimb, and Akira Kohyama. Mechanical properties

of friction welds of RAFs (JLF-1) to SUS 304 steels as measured by the acoustic emission technique. *Fusion Engineering and Design*, 81:945–50, 2006.

[3] T. Stepinski (editor), T. Olofsson, and E. Wennerström. Inspection of copper canisters for spent nuclear fuel by means of ultrasound. Technical Report TR-06-47, Signals and Systems, Department of Technical Sciences, Uppsala University, December 2006.

[4] K. Dahlgren. Sensor array for acoustic emission. Master's thesis, Department of Engineering Sciences, Uppsala University, 2007.

[5] G. Hampson. *Implementing Multi-Dimensional Digital Hardware Beamformers*. PhD thesis, Department of Digital Systems, Monash University, August 1997.

[6] H. L. Van Trees. *Optimum Array Processing, Part IV of Detection, Estimation and Modulation theory*. John Wiley & Sons, Inc, New York, 2002.

[7] H. P. Raabe. Fast beamforming with circular receiving arrays. *IBM J. Res. Develop.*, July 1974.

[8] C. P. Matthews and M. D. Zoltowski. Eigenstructure techniques for 2-d angle estimation with uniform circular arrays. *IEEE Transactions on Signal Processing*, 42:2395–2407, 1994.

[9] S. C. Chan and Carson K. S. Pun. On the design of digital broadband beamformer for uniform circular array with frequency invariant characteristics. *Circuits and Systems, IEEE International Symposioum on*, 1:693–696, 2002.

[10] S. C. Chan and H. H. Chen. Theory and design of uniform concentric circular arrays with frequency invariant characteristics. *Acoustics, Speech and Signal Processing, IEEE Proceedings*, 4:805–808, 2005.

Chapter 3

Copper Characterization Using Resonant Ultrasound Spectroscopy

by Marcus Engholm

3.1 Introduction

The relationship between grain size and ultrasonic attenuation is well known and has been treated extensively in the literature. In our previous report [1] this relationship was examined experimentally on a set of copper blocks of various grain sizes provided by the Corrosion and Metals Research Institute (KIMAB). Some discrepancies were observed concerning the attenuation as a function of grain size and some of the samples also proved to be anisotropic, which means that the material properties, such as wave velocity and attenuation, were dependent on the direction of propagation. In this work these samples were examined further to see if an alternative approach could be found. A method called resonant ultrasound spectroscopy (RUS) was used to examine the elastic properties of the samples using both isotropic and anisotropic assumptions.

In this report the theory of RUS is described along with some practical issues concerning the method. The elastic properties of the materials are compared with grain size measurements. The importance of the distribution of the grain sizes is also stressed, along with measurements of not only the mean grain size and attenuation, but also the distribution of each parameter.

3.2 Methods for grain size estimation

In this section the two methods used for grain size evaluation in this project are briefly introduced.

3.2.1 Intercept method

One of the most common and accepted methods for grain size estimation from a cross-section of a specially prepared sample is the linear intercept method, also known as Heyn's intercept method. By counting the number of grain boundaries that intercept random straight lines on a representative area of the sample, an average grain size can be calculated [2]. To achieve a reasonable statistical accuracy, at least three different areas of the sample should be analyzed, and the number of grain boundaries that are intercepted should be at least 50 on each area. The intercept counts from each line can be used to calculate the intercept distribution.

3.2.2 Attenuation

Ultrasonic attenuation is related to the grain size of a material due to scattering of elastic waves. Generally, larger grains result in a higher attenuation of ultrasound. The relationship between attenuation and grain size can be explained by three different processes, each relevant for a certain frequency range [3]:

$$\text{for } \lambda \gg 2\pi\overline{D},\ \alpha \propto Tf^4 \tag{3.1}$$

$$\text{for } \lambda < 2\pi\overline{D} \text{ or } \lambda \cong \overline{D},\ \alpha \propto \overline{D}f^2 \tag{3.2}$$

$$\text{for } \lambda \ll 2\pi\overline{D},\ \alpha \propto 1/\overline{D}. \tag{3.3}$$

where $\overline{D}$ is the average grain diameter, λ is the wavelength, R is the grain radius, f is frequency and

$$T = \frac{4\pi}{3}\frac{\langle R^6\rangle_{\text{av}}}{\langle R^3\rangle_{\text{av}}}.$$

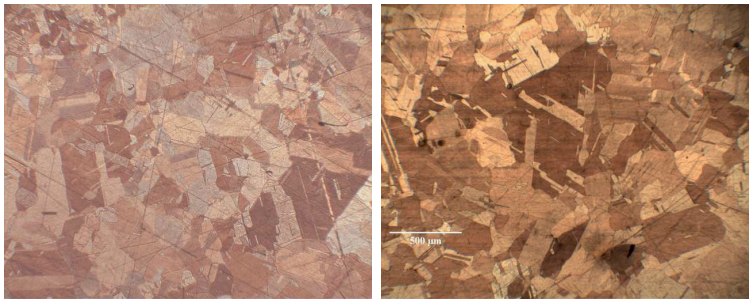

Figure 3.1: Figure shows two images from the $5.5\,cm^2$ slice of the sample 8423.

Where $\langle R^n \rangle_{\text{av}}$ is the n-th central moment[1]. Most ultrasonic inspections are carried out in the frequency region described by Eq. 3.1, the so called *Rayleigh region*. Since higher order moments depend on the width of the grain size distribution, this shows that the attenuation calculated from a single grain size average is only valid for a narrow grain size distribution. To calculate the attenuation of materials with broader grain size distributions, the higher order moments of the grain radii need to be determined.

3.3 Grain size estimation using the intercept method

The grain size is mostly stated as a mean value of a preferably large number of measurements. Previous work, reported in [1], showed some discrepancies between attenuation and grain size. Since the relationship between attenuation and grain size is nonlinear, the grain size distribution in a given sample can provide additional information. The samples were therefore re-evaluated to get an estimate of the grain size variance. An advantage of the linear intercept method used for the estimation is that it also produces the statistical distribution of the intercepts. To compare the width of the probability distributions for the investigated samples, the sample standard deviation was calculated.

Table 3.1 shows the results of the re-evaluations compared to the previous estimates. The second column of the table is the mean intercept length, but since there was a large discrepancy compared to the KIMAB estimates, it is assumed that a correction factor was used. A commonly used factor in the literature is 1.56, which transforms the one dimensional intercepts to a spherical radius. This correction is only valid for spherical grains, though it is doubtful that it is justified for our samples. The spherical grain radius is presented in column 4, which shows a better correlation with the previous KIMAB estimates. There is still a significant discrepancy between the estimates, which could be explained by the limited number of microscope images and the small area from which these were taken. Only $5.5\,cm^2$ slices was used from each sample from which three microscope images were taken. Areas having significantly different grain size could be observed on a single slice which suggests that several sample slices are needed to achieve an accurate estimate. Two microscope images taken from the same sample slice where regions with both large and small grains are present are shown in Figure 3.1.

It should be noted that the presented standard deviations are not the standard deviations of the actual grain size distribution, but the standard deviation of the measured intercept lengths. In order to estimate the grain size distributions, further calculations have to be performed which is beyond the scope in this work. For more information on the topic see, for example [4] or [5].

[1]The n-th central moment is defined as $\int (R - \overline{D}/2)^n P(R) dR$, where $P(R)$ is the grain size distribution.

Table 3.1: Grain size estimate comparison

Specimen	Heyn's	Heyn's std.dev	Heyn's corr.	KIMAB
Cu197	121.93	54.72	190.21	197.00
Cu214	73.06	11.40	113.97	214.00
Cu282	110.42	23.79	172.26	282.00
8422	154.46	26.67	240.96	305.00
8423	93.20	26.49	145.39	112.00
8425	55.61	7.88	86.75	81.00
8426	169.98	30.32	265.17	286.00
8429	169.90	45.28	265.04	320.00

3.4 Attenuation measurements

The above mentioned difficulty related to grain size distribution motivated a more detailed investigation of the ultrasonic attenuation. To see whether a variance also could be observed in the attenuation, similar to that found from the grain size estimates using the intercept method, the attenuation was measured on small samples of each copper block. The samples were taken close to the area used for the microscopic images. Figure 3.2 shows en example of the back-wall echo amplitude, measured over the area of two samples using a 10 MHz focused transducer. The images show a fairly large variance in amplitude over the areas.

To enable quantitative analysis, the mean attenuation and the variance of the sample distribution of the attenuation were calculated for each sample. The results are presented in Figure 3.3, which shows the amplitude of the received echo as a function of the estimated grain size for the present and previous measurements. The amplitude of the echo in arbitrary units is used instead of the attenuation (this enables a relative comparison only). In Figure 3.3a the spread in both the echo amplitude and grain size shows a large distribution overlap for most of the samples. The Figure 3.3 shows a relatively strong correlation between the attenuation and the grain size for both measurements. It seems that a better agreement between the previous attenuation measurements with the KIMAB grain size estimates (cf Figure 3.3b and d), while the new attenuation measurements agree better with the new grain size estimates (cf Figure 3.3b and d). The good correlation in Figure 3.3a is not surprising since both the attenuation measurement and the grain size estimation were performed on two adjacent areas of the sample.

3.5 Resonant ultrasound spectroscopy

Knowledge of the frequencies at which an object is resonating is a valuable source of information. Each of the resonance frequencies correspond to a certain vibration mode or resonance mode. Many of the material properties of an object, such as geometric and elastic properties, directly affect its resonance modes and frequencies. It is therefore reasonable to assume that if a sufficient number of resonance frequencies could be determined, it would be also possible to determine a set of material properties that are most likely to govern these resonance frequencies.

Calculating the resonance frequencies of an arbitrary object with certain elastic properties is fairly straightforward using numerical methods. The reverse problem is an entirely different matter, because there is no unique set of material properties for a given set of resonance frequencies. Consequently, it is necessary to resort to non-linear optimization procedures to find the best possible agreement between the material properties and the measured resonance

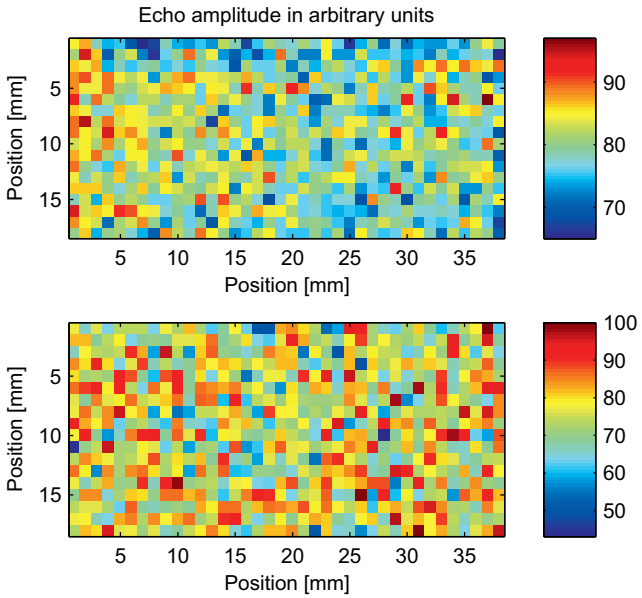

Figure 3.2: Amplitude of the back wall echo as a function of position for samples Cu197 (top) and 8422 (bottom).

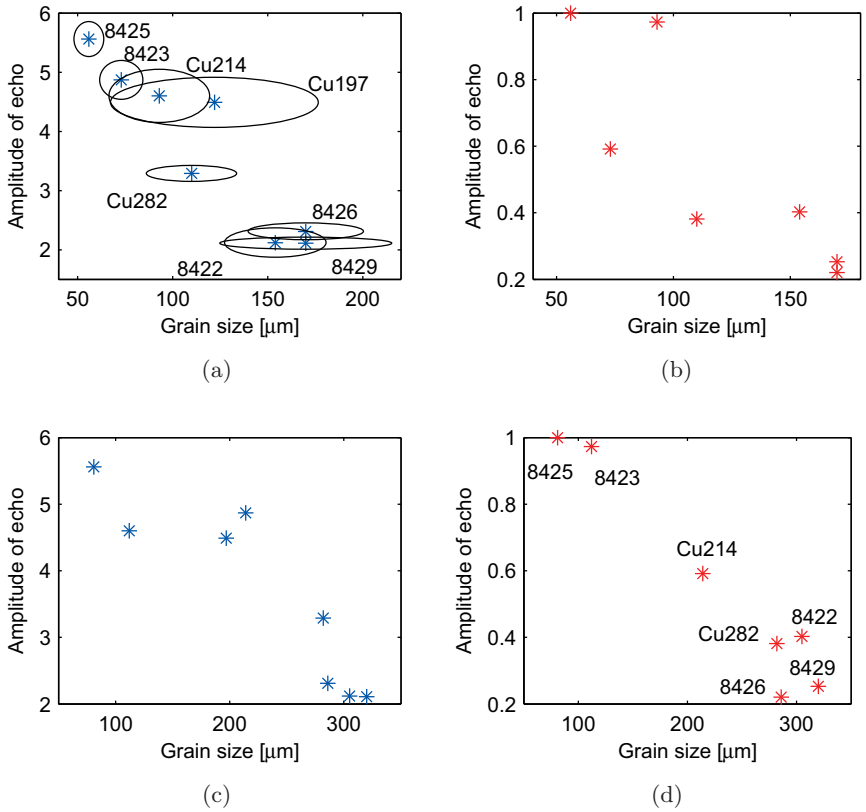

Figure 3.3: Comparison of the echo amplitude as a function of grain size. a) and b) show the new and the previous attenuation measurements, respectively, as a function of the new grain size estimates. c) and d) show the new and the previous attenuation measurements, respectively, as a function of the KIMAB grain size estimates. Ellipses in a) show the sample spread equal to two standard deviations.

frequencies.

The experimental setup needed to perform resonance frequency measurements differs from the standard ultrasonic equipment used for non-destructive testing and evaluation, but is relatively simple and requires few components.

3.5.1 Calculation of the resonance frequencies

General theory

Analytical solutions to the problem of calculating the resonance frequencies of an object exists for only a few special cases. For general geometries it is necessary to use numerical approximations. Finite element analysis (FEA) is one possible approach, which can be applied to very general problems. The disadvantage of commercial FEA software is that it is not always possible to take advantage of obvious symmetries and other simplifications which can greatly increase the computational efficiency. The FEA software evaluated for this application proved to be too slow to be practically useful. Instead another method commonly used in RUS applications was evaluated and selected, the so called Rayleigh-Ritz method. Assuming that the object can be seen as a freely vibrating body, that is, having stress-free surfaces, the problem can be solved using the Rayleigh-Ritz variational method as described below. Following the derivation presented in [6] the Lagrangian L is written

$$L = \iiint_V (E_k - E_p)\, dV \tag{3.4}$$

where E_k is the kinetic energy and E_p is the potential energy. The kinetic energy is given by

$$E_k = \frac{1}{2} \sum_i \rho \omega^2 u_i^2 \tag{3.5}$$

where i runs from 1 to 3, corresponding to the x, y and z direction, ρ is the density and u_i is the displacement. The potential energy is given by

$$E_p = \frac{1}{2} c_{i,j,k,l} \frac{\partial u_i}{\partial x_j} \frac{\partial u_k}{\partial x_l} \tag{3.6}$$

where $c_{i,j,k,l}$ is the linear elasticity tensor with i, j, k, l representing the x, y or z directions, respectively. A simplified notation can be used for the elasticity tensor:

$$\begin{array}{lll} 11 \rightarrow 1 & 22 \rightarrow 2 & 33 \rightarrow 3 \\ 23 \rightarrow 4 & 13 \rightarrow 5 & 12 \rightarrow 6 \end{array}$$

and through symmetry

$$32 \rightarrow 4 \quad 31 \rightarrow 5 \quad 21 \rightarrow 6.$$

Without going further into the details regarding the theory of linear elasticity, which is described in standard mechanics textbooks, it is noted that for linear isotropic materials the number of independent constants are reduced to two, c_{11} and c_{44} with $c_{12} = c_{11} - 2c_{44}$, where $c_{11} = c_{22} = c_{33}$, $c_{44} = c_{55} = c_{66}$, $c_{12} = c_{21} = c_{31} = c_{13} = c_{23} = c_{32}$, and the rest of the constants are 0.

The minimum of the Lagrangian will correspond to resonances of the object. Finding the minima results in a variational problem which can be solved using the Rayleigh-Ritz method. If the displacement vector u_i is expanded using a complete set of functions Φ_λ

$$u_i = \sum_\lambda a_{i\lambda}\Phi_\lambda. \tag{3.7}$$

Φ_λ can be chosen to be, for example, Legendre polynomials that are computationally very efficient for some object shapes, but a more flexible basis is [6]

$$\Phi_\lambda = x^l y^m z^n. \tag{3.8}$$

Following the derivation from Migliori [6], the minimization problem results in the eigenvalue equation

$$\omega^2 \mathbf{E}\overline{a} = \mathbf{\Gamma}\overline{a}. \tag{3.9}$$

The elements of the $\mathbf{E}$ and $\mathbf{\Gamma}$ matrices are calculated as

$$E_{\lambda i\lambda' i'} = \delta_{ii'} \iiint_V \Phi_\lambda \rho \Phi'_\lambda dV \tag{3.10}$$

$$\Gamma_{\lambda i\lambda' i'} = \sum_{j,j'} c_{iji'j'} \iiint_V \frac{\partial \Phi_\lambda}{\partial x_j}\frac{\partial \Phi_{\lambda'}}{\partial x_{j'}} dV. \tag{3.11}$$

The eigenvalues ω^2 of Eq. (3.9) represent the square of the angular resonance frequencies. The eigenvectors $\overline{a}$ can be used in Eq. (3.7) to calculate the displacements for each resonance mode.

The accuracy of the approximation is determined by limiting the order of the polynomials in Eq. (3.8) such that

$$l + m + n < N. \tag{3.12}$$

The exact solution to the problem is found when $N \to \infty$. $N = 10$ is a reasonable start, but significant improvements in accuracy have been seen up to $N = 14$. Each increment of N results in a considerable increase of computational load.

Sample symmetry

Utilizing known symmetries of the samples can dramatically reduce the computational load. The copper block samples used in this work are rectangular parallelepipeds having sides $2d_1$, $2d_2$, and $2d_3$, which resulted in the modified Eq. (3.10) and (3.11) that include volume integrals of the form [6]

$$f(p,q,r) = \iiint_V x^p y^q z^r dV = \tag{3.13}$$

$$\frac{8 d_1^{(p+1)} d_2^{(q+1)} d_3^{(r+1)}}{(p+1)(q+1)(r+1)}. \tag{3.14}$$

Since the above integration is performed over symmetric limits its result, for each case when $f(p,q,r)$ is an odd function, is equal to zero. This makes it possible to rearrange Γ into a block diagonal matrix composed of eight blocks. Eq. 3.9 is calculated through matrix diagonalization, which is numerically performed in N^3 steps for $N \times N$ matrix, and therefore eight smaller matrices will be computed much faster than one large.

3.5.2 Parameter estimation

As mentioned above, the unique solution to the inverse problem that consists in finding the material parameters from a set of resonance frequencies, does not exist. However, a solution to the direct problem, as presented in section 3.5.1, can be very helpful. It can be used in the non-linear optimization to find the set of material properties that are hopefully closest to the true values. Assuming that a set of resonance frequencies g_i has been acquired, where i is the number of the resonance mode, the parameter vector $\overline{p}$ is sought, which produces a set of resonance frequencies $f_i(\overline{p})$ that minimizes the error function

$$F = \sum_{i=1}^{N=1} \left(\frac{f_i(\overline{p}) - g_i}{g_i} \right)^2. \tag{3.15}$$

A suitable algorithm for solving this type of non-linear least-square optimization problems is the Levenberg-Marquardt method [6]. Detailed derivation and description of this method can be found in most textbooks on non-linear optimizations, for example [7]. Implementations of this method is widely available. In this work the implementation in the Optimization Toolbox in Matlab was used. The Levenberg-Marquardt is the default algorithm used in the `lsqnonlin` function. Some Levenberg-Marquardt implementations, such as `lsqnonlin`, provide the possibility to approximate the derivatives of the error function through finite differencing. Although convenient, this is of course computationally less efficient since each step requires several function evaluations. Luckily, it is fairly straight forward to calculate the derivatives with respect to the parameters from the eigenvalue equation (3.9) analytically:

$$\frac{\partial \omega_i^2}{\partial p} = \frac{1}{\overline{a}^T E \overline{a}} \overline{a}^T \left[\frac{\partial \mathbf{\Gamma}}{\partial p} - \omega_i^2 \frac{\partial \mathbf{E}}{\partial p} \right] \overline{a}. \tag{3.16}$$

The parameters (denoted p for generality) usually include the elastic constants, for example c_{11} or c_{44}, or the geometric dimensions. In this work only the elastic constants were considered. Since $\mathbf{E}$ is independent of the elasticity the derivates can be written as

$$\frac{\partial f_i}{\partial p} = \frac{1}{8\pi^2 f_i \overline{a}^T \mathbf{E} \overline{a}} \overline{a}^T \frac{\partial \mathbf{\Gamma}}{\partial p} \overline{a}. \tag{3.17}$$

The measurement procedure results in a frequency spectrum containing the excited modes. For low attenuating materials having small geometry errors and a flat spectrum with sharp isolated peaks, the resonance frequency can with high accuracy be found at the maximum of the resonance peak. For samples having overlapping modes, for example where a mode appears as a bump on the slope of a stronger mode, this does not give an accurate estimate. Other problems can be encountered for the materials with high attenuation and inadequate suspension. For these cases a more sophisticated nonlinear least-square fitting routine of Lorentzian functions is required. The following spectrum model was used to estimate the resonance frequencies [8]:

$$A(f) = B_0 + B_1(f - f_0) + \sum_{n}^{N} \frac{C_n + D_n(f - f_0)}{(f - f_n)^2 + \frac{1}{4}\Gamma_n^2}. \tag{3.18}$$

where B_0 and B_1 model the baseline, C_n the amplitude of peak n, D_n the skewness, Γ_n the full width at half the amplitude, and f_n the resonance frequency. Although the model Eq. 3.18 is capable of separating overlapping modes, the nonlinear fitting routine is not always able to make a good fit for small resonances, especially those close to larger resonance peaks.

Estimates of the confidence intervals serve as a useful indicator of problematic estimates when dealing with large number of resonances. The confidence interval can be estimated numerically

by estimating the Hessian of the objective function, in this case the least-square error between the model in Eq. 3.18 and the measured spectrum. The `nlinfit` function in the Matlab Statistics toolbox was used in this work for calculating the confidence intervals.

3.5.3 Measurement setup

The measurements were performed using Agilent-4395A network analyzer in through-transmission setup as illustrated in Figure 3.4. Two transducers were placed on opposite sides of the sample under inspection, one served as a transmitter and the second as a receiver. The output port of the network analyzer excited the transmitter with a continuous wave swept over a preselected frequency range. The frequency range included the lowest 30 - 40 resonance modes of the copper blocks. The receiving transducer was connected to the input of the network analyzer. The network analyzer was used to automatically acquire the amplitude for each frequency to form a spectrum. Since the network analyzer has $50\,\Omega$ impedance at its input and output ports, and limited driving capabilities, separate amplifiers were used on both the transmitting side and the receiving side. Instead of using a network analyzer, it is possible to use a computer controlled function generator and a lock-in amplifier to perform the measurement. This is a much less expensive solution if a network analyzer is not available.

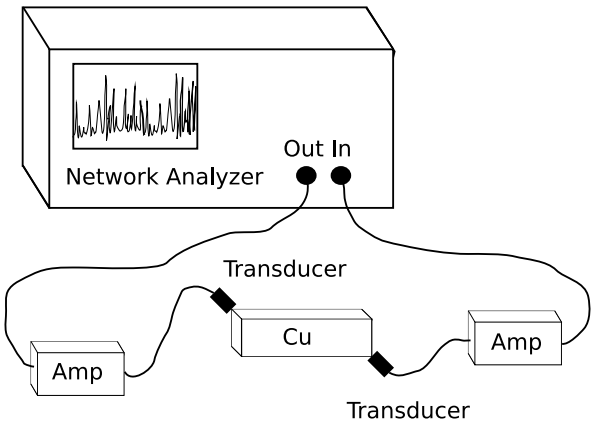

Figure 3.4: Measurement setup showing the ports of the network analyzer used for spectrum acquisition. Two external amplifiers are used for the transducers. The transducers are weakly coupled to the sample at its corners.

Transducers and sample mounting

The most important properties of piezoelectric transducers are their resonance frequencies. If the transducers' resonances overlap the sample's peaks in the frequency band used for spectrum acquisition it can be difficult to identify the samples' resonances. Closely placed overlapping resonances also distort the resonance peaks decreasing the accuracy of the frequency estimation of that mode. Migliori [6] describes several approaches to overcome this problem. The problem is more complex for small samples since it is more difficult to design transducers with resonances higher than those of the sample. For larger samples, having several resonances below $\sim 300\,kHz$, this is normally not an issue. In this work only lower frequency bands were considered, for which small piezoelectric transducers were sufficient. The two transducers used in the setup were identical and consisted of thin piezoelectric circular elements and a thin planar frontal protective layer. Transducers with conical tips were also evaluated, but the cones caused the frequency spectrum of the transducers to become more complex and also slightly lower in frequency.

This was not compensated by an increased sensitivity, making the overall performance of these transducers worse compared to the planar transducers.

Access to a priori information is of course desirable in any estimation problem. In this application the number of resonance frequencies that can be accurately estimated and identified is what ultimately determines the accuracy of the parameter estimate for a given setup. This leads to the problem of mode excitation. Each resonance has a unique displacement mode shape, which is determined by the geometry of the sample and its elastic properties. The displacement at each point on the surface of the sample for a particular resonance mode determines the efficiency with which the transducers can excite and detect that mode. It has been shown [6] that for parallelepipeds the most modes are excited and received if the transducers are coupled to the corners of the object. Studying the mode shapes from numerical calculations can be of assistance when identifying the resonance peaks. The resonances with very small particle displacements at the transducer positions are likely to have very low resonance peaks in the spectrum. A good way to start the identification process is limiting the fitting procedure to only the first few resonances. The preliminary parameter estimates, obtained in this way, can then be used to calculate the higher resonance frequencies and thereby greatly simplify the identification process.

Another issue that has to be considered is the assumption that the sample has zero stress at its surfaces. This affects both the sample suspension and the transducer mounting. How to suspend the samples depends on the weight of the sample. Small samples can usually be suspended by the transducers but larger samples need further support. In this work the blocks were suspended with thin strings of steel or nylon.

The transducers need to apply a certain pressure to the sample to achieve good coupling. Applying too much pressure results in less accurate estimates since the zero stress boundary condition is no longer valid. The performance of different measurement setups can be evaluated by comparing the confidence interval of the estimates, for example, a bad sample suspension may result in a broader confidence interval.

3.5.4 Correlation between grain size and elastic properties

Isotropic case

Figure 3.5 shows the estimated shear modulus as a function of the recent grain size estimates of the blocks. The bars represent the confidence interval of the estimates. The estimates of the bulk modulus as a function of grain size are presented in Figure 3.6. The reason why the accuracy of the shear modulus is so much higher than that for the bulk modulus can be explained by the high sensitivity of the resonance frequencies to changes in the shear modulus.

The finest grained sample, the 8425 (the fine grain located at most left in Figures 3.5 and 3.6), has a significantly lower shear modulus that the others. This sample showed a strange behaviour during the measurements in that it was particularly difficult to acquire a usable spectrum, which reduced the number of usable resonance frequencies in the estimation process. This can to some degree be seen in the confidence interval of the estimate.

Anisotropic case

Grain shapes, size and orientation can make the material more or less anisotropic. If a material has a grain orientation that is more probable than others, the material will be globally anisotropic [9]. This makes both wave velocity and attenuation dependent on the direction. Resonant ultrasound spectroscopy is not limited to isotropic materials. Anisotropic symmetries can be

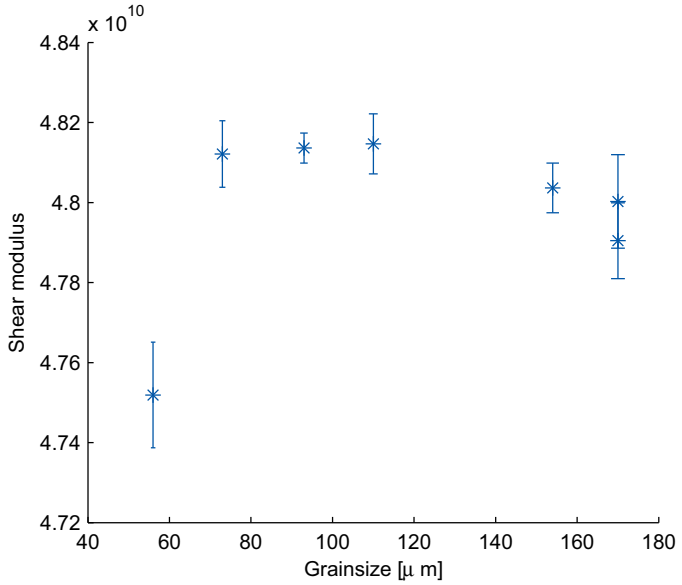

Figure 3.5: Shear modulus as a function of grain size for the blocks. Finest grain sample has a considerably lower modulus.

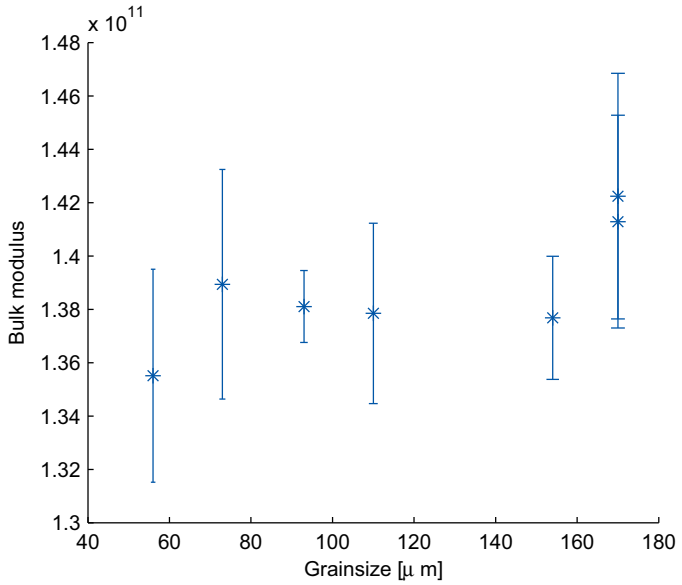

Figure 3.6: Bulk modulus as a function of grain size for the blocks. Confidence in bulk modulus is too low to draw any conclusions.

included in the model, which can then be used to estimate a full set of elastic moduli. The simplest form of anisotropy, cubic symmetry, is represented by three independent elasticity parameters. This might not be a good model in terms of symmetry and crystal orientation, but it can be used as an indicator that the material is more or less anisotropic. For isotropic materials the relation $c_{11} = 2c_{44} + c_{21}$ holds, but for cubic symmetry c_{11} is independent. An anisotropy parameter is introduced as a measure of anisotropy, which is defined as [10]

$$F_a = \left| 1 - \frac{2c_{44}}{c_{11} - c_{12}} \right|$$

The three parameters c_{11}, c_{12} and c_{44} can be determined through RUS measurements. If the material is completely isotropic, this factor should be zero.

In Figure 3.7 the anisotropy parameter is presented as a function of grain size. Samples characterized by larger grain size tend to have a higher anisotropy parameter. The sample 8426 has the highest anisotropy parameter, which might explain why it distinguishes itself in the attenuation measurements in Figure 3.3d.

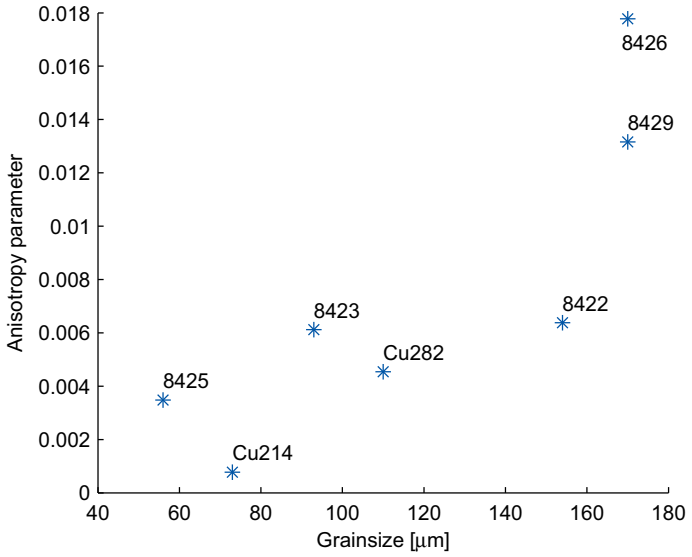

Figure 3.7: Anisotropy parameter as a function of grain size. The anisotropy parameter is calculated from RUS measurements of the elasticity parameters c_{11}, c_{12} and c_{44}.

3.6 Discussion

Correlation between grain size, ultrasonic attenuation and elastic moduli was studied. A number of copper samples from SKB's canister material with artificially grown grains was investigated using resonant ultrasound spectroscopy (RUS) and classical pulse-echo ultrasound.

An experimental method for estimating elastic moduli from the RUS measurements was developed. The accuracy of the bulk modulus estimates is too low to draw any definite conclusions. The shear modulus that has been measured with a satisfying accuracy does not show any well pronounced correlation with the grain size. The investigated samples show differences in shear modulus that are statistically certain, but the cause of the differences is yet to be explained. Most notable is the finest grain sample (8425), which has a significantly lower shear modulus

than the others. An anisotropy index based on a simple cubic anisotropy model was evaluated. The results show a well pronounced correlation between the anisotropy index and grain size.

A simple method of evaluating ultrasonic attenuation based on the pulse-echo amplitude measurements was applied and a clear correlation was found between the measured amplitudes and the grain size. A considerable local variations in pulse amplitudes were observed indicating a high degree of inhomogeneity in the samples.

Summarizing, the results show that while the elastic properties of the investigated material are relatively constant the ultrasonic attenuation exhibits a considerable variation, which is apparently correlated with grain size.

Bibliography

[1] Ping Wu and T. Stepinski. Inspection of copper canisters for spent nuclear fuel by means of ultrasound - evaluation of ultrasonic attenuation in copper. Technical Report TR-06-02, SKB, 2006.

[2] H. Modin and S. Modin. *Handbok i metallmikroskopering.* Meritförlaget, 1968.

[3] E.P. Papadakis. Ultrasonic attenuation caused by scattering in polycrystalline metals. *Journal of the Acoustical Society of America*, 37(4):711 – 717, 1965.

[4] E.P. Papadakis. From micrograph to grain-size distribution with ultrasonic applications. *Journal of Applied Physics*, 35(5), 1963.

[5] D. Nicoletti and A. Anderson. Determination of grain-size distribution from ultrasonic attenuation: transformation and inversion. *Journal of the Acoustical Society of America*, 101(2), 1997.

[6] A. Migliori. *Resonant Ultrasound Spectroscopy.* Wiley, New York, NY, 1997.

[7] H. Ramsin. *Ickelinjär optimering.* LiberLaromedel, 1976.

[8] B.J. Zadler, J.H.L. Le Rousseau, J.A. Scales, and M.L. Smith. Resonant ultrasound spectroscopy: theory and application. *Geophysical Journal International*, 156(1):154 – 69, 2004/01/.

[9] E. P. Papadakis. *Physical Acoustics - Principles and Methods Volume IV - Part B*, chapter 15 - Ultrasonic Attenuation Caused by Scattering in Polycrystalline Media. Academic Press, New York, 1968.

[10] P. S. Spoor, J. D. Maynard, and A. R. Kortan. Elastic isotropy and anisotropy in quasicrystalline and cubic alculi. *Phys. Rev. Lett.*, 75(19):3462–3465, Nov 1995.

Chapter 4

On Design of Input Signals for Ultrasonic Array Imaging

by Tomas Olofsson

4.1 Introduction

Traditionally, array systems are designed with classical beamforming in mind, meaning that the design of the array system must respect the limitations that classical beamforming imposes. Namely, sub-wavelength array pitches and small element sizes in order to avoid artifacts and resolution loss. Conventional delay-and-sum (DAS) array imaging is based on a geometrical optics approach where the array elements are treated as point sources. Some well known problems with such an approach to ultrasonic imaging are: the array pitch must be lower than half the wavelength of the transmitted pulse to avoid grating lobes, and the finite-size of the array elements are not accounted for.

Recently it has been shown that model based methods can compensate for both diffraction effects due to finite size of the array elements [1] as well as grating lobes due to under-sampled array setups [2]. The better performance of these methods is due to the fact that more information of the imaging system is used in the imaging processes compared to conventional DAS imaging. The performance of these methods are mostly determined by the signal-to-noise ratio (SNR) at the particular region if interest. That is, if the signal energy at a region is sufficient then the model based methods can compensate for the diffraction effects etc. and very high resolution images can be obtained.

This chapter contains an edited version of our papers [3, 4]. Below, we will study the Bayesian linear minimum mean squared error (LMMSE) estimator discussed formerly in [2]. The aim is to show that it offers a useful tool for designing and evaluating ultrasonic array systems. This is due to the fact that these methods provides a natural measure of the accuracy of the estimates. In particular we will introduce a method to design input signals, driving an array system, so that the expected error of the LMMSE estimator is minimized for chosen set of control points.

This chapter is organized as follows: In Section 4.2 the linear model based on the impulse response method is introduced and in Section 4.3 the optimal LMMSE beamformer is presented. Section 4.4 presents a performance criterion and suggests an optimization strategy. Some simulation examples are then shown in Section 4.5, and finally in Section 4.6 a discussion is given.

4.2 A Discrete Linear Model of the Imaging System

Consider an array with K transmit elements and L receive elements and contributions from a single observation point, $\mathbf{r}$. Let $o(\mathbf{r})$ denote the scattering strength at $\mathbf{r}$ and $u_k(t)$ the input signal for the kth transmit element. Furthermore, let $h_k^{ef}(t)$ and $h_l^{eb}(t)$ denote the forward- and backward electrical impulse responses of the transducers, respectively. Then the received signal from the lth receive element, $y_l(\mathbf{r},t)$, can be expressed

$$\begin{aligned} y_l(\mathbf{r},t) = \sum_{k=0}^{K-1} & h_k^{\mathrm{SIR}}(\mathbf{r},t) * h_k^{\mathrm{ef}}(t) * u_k(t) o(\mathbf{r}) * \\ & h_l^{\mathrm{SIR}}(\mathbf{r},t) * h_l^{\mathrm{eb}}(t) + e_l(t), \end{aligned} \tag{4.1}$$

where $*$ denotes temporal convolution, $e_l(t)$ is the noise for the lth receive element, and $h_k^{\mathrm{SIR}}(\mathbf{r},t)$ the forward spatial impulse response (SIR) for the kth transmit element, and $h_l^{\mathrm{SIR}}(\mathbf{r},t)$ the backward SIR for the lth receive element. We can gather the impulse responses modeling the excitation and wave propagation to the scatterer:

$$h^{\mathrm{f}}(\mathbf{r},t) = \sum_{k=0}^{K-1} h_k^{\mathrm{SIR}}(\mathbf{r},t) * h_k^{\mathrm{ef}}(t) * u_k(t) \tag{4.2}$$

Similarly, we can gather the impulse responses that model propagation from that scatterer and back to the transducer as well as reception as

$$h_l^{\mathrm{b}}(\mathbf{r},t) = h_l^{\mathrm{SIR}}(\mathbf{r},t) * h_l^{\mathrm{eb}}(t). \tag{4.3}$$

Using $h^{\mathrm{f}}(\mathbf{r},t)$ and $h_l^{\mathrm{b}}(\mathbf{r},t)$, we can express the total, or *system impulse response* for the lth receive element as

$$h_l(\mathbf{r},t) \triangleq h^{\mathrm{f}}(\mathbf{r},t) * h_l^{\mathrm{b}}(\mathbf{r},t). \tag{4.4}$$

and the relation in eq. (4.1) can be compactly written as

$$y_l(\mathbf{r},t) = h_l(\mathbf{r},t)o(\mathbf{r}) + e_l(t). \tag{4.5}$$

A time-discrete version of (4.1) is obtained by sampling the impulse responses and using discrete time convolutions and then place all discrete impulse responses into a matrix (see [2] for details), from a target at an observation point at $\mathbf{r} = (x_m, z_n)$, can then be expressed as[1].

$$\mathbf{y}_l = \mathbf{h}_m^{(n,l)}(\mathbf{O})_{m,n} + \mathbf{e}, \tag{4.6}$$

where the vector $\mathbf{h}_m^{(n,l)}$ is the double-path discrete impulse response for the lth receive element, $\mathbf{O}$ is a $M \times N$ matrix that represents the scattering amplitudes in the ROI, and the notation $(\mathbf{O})_{m,n}$ denotes element (m,n) in $\mathbf{O}$. If we collect all MN system impulse responses for the lth receive element into a matrix $\mathbf{P}_l$ and then append all L $\mathbf{P}_l$:s according to [2]

$$\begin{aligned}\mathbf{y} =& \begin{bmatrix}\mathbf{P}_0\\ \mathbf{P}_1\\ \vdots\\ \mathbf{P}_{L-1}\end{bmatrix}\mathbf{o} + \begin{bmatrix}\mathbf{e}_0\\ \mathbf{e}_1\\ \vdots\\ \mathbf{e}_{L-1}\end{bmatrix}\\ =& \mathbf{P}\mathbf{o} + \mathbf{e},\end{aligned} \tag{4.7}$$

where $\mathbf{y}$ is the vectorized B-scan data, $\mathbf{o}$ is the vectorized image of scattering strengths. The *propagation matrix*, $\mathbf{P}$, in (4.7) describes both the transmission and the reception process for an arbitrary excited array. Note that $\mathbf{P}$ is a function of the K arbitrary discrete input signals $\mathbf{u}_k$. The model (4.7) is, therefore, very general in the sense that any type of input signals can be considered within the limitations of the hardware that is used. In [2], the elements in $\mathbf{o}$ were scattering strengths at positions on a dense grid. In the input design discussed here we consider instead only a reduced set of points. Below we call these *control points*.

For example, the length of the input signals are typically limited by the finite length of the transmit buffer, and the signal amplitudes are limited by digital-to-analog converters and the amplifiers used.

4.3 The Optimal Linear Estimator

The optimal linear estimator is found by minimizing a mean squared error criteria resulting in the LMMSE estimator, $\mathbf{K}_{\mathrm{LMMSE}}$, given by [2]

$$\begin{aligned}\mathbf{K}_{\mathrm{LMMSE}} &= \arg\min_{\mathbf{K}} \ \mathrm{E}\{\|\mathbf{o} - \mathbf{K}\mathbf{y}\|^2\}\\ &= \mathbf{C}_{\mathrm{o}}\mathbf{P}^T(\mathbf{P}\mathbf{C}_{\mathrm{o}}\mathbf{P}^T + \mathbf{C}_{\mathrm{e}})^{-1}.\end{aligned} \tag{4.8}$$

[1]The transducer elements are lined up in the x-direction (azimuth) and z is the depth. For simplicity, in this work we only consider points in the plane $y = 0$ (elevation)

where $\mathrm{E}\{\cdot\}$ is the expectation operator, and where we assumed that $\mathbf{o}$ and $\mathbf{e}$ are zero mean and mutually independent with covariance matrices $\mathbf{C}_\mathrm{o} = \mathrm{E}\{\mathbf{o}\mathbf{o}^T\}$ and $\mathbf{C}_\mathrm{e} = \mathrm{E}\{\mathbf{e}\mathbf{e}^T\}$, respectively. Furthermore, by also assuming that the covariance matrices $\mathbf{C}_\mathrm{o}$ and $\mathbf{C}_\mathrm{e}$ have the form $\mathbf{C}_\mathrm{o} = \sigma_\mathrm{o}^2\mathbf{I}$ and $\mathbf{C}_\mathrm{e} = \sigma_\mathrm{e}^2\mathbf{I}$, Eq. (4.8) reduces to

$$\mathbf{K}_{\mathrm{LMMSE}} = \mathbf{P}^T(\mathbf{P}\mathbf{P}^T + \mu\mathbf{I})^{-1}, \tag{4.9}$$

with $\mu = \sigma_\mathrm{e}^2/\sigma_\mathrm{o}^2$. The optimal linear beamformer (4.8) has been shown to successfully be able to compensate for finite-sized array elements [1] as well as to suppress side- and grating lobes [2] if the SNR is sufficient.

4.4 The Performance Criterion

It is well known [5] that if the measurement noise and the prior distribution of $\mathbf{o}$ are both Gaussian then the distribution for the reconstruction error, $\mathbf{s}\epsilon = \hat{\mathbf{o}}_{\mathrm{LMMSE}} - \mathbf{o}$, for the LMMSE estimator is Gaussian with covariance matrix $\mathbf{C}_\epsilon$. The expected mean-squared errors at each observation point are given by the corresponding diagonal elements in $\mathbf{C}_\epsilon$. For example, the performance of the LMMSE estimator can be visualized by organizing the diagonal elements $\mathrm{diag}(\mathbf{C}_\epsilon)$ into an $M \times N$ error image $\mathbf{E}_\epsilon$.

The error covariance matrix $\mathbf{C}_\epsilon$ is given by [5]

$$\begin{aligned}\mathbf{C}_\epsilon &= \mathbf{C}_\mathrm{o} - \mathbf{C}_\mathrm{o}\mathbf{P}^T(\mathbf{P}\mathbf{C}_\mathrm{o}\mathbf{P}^T + \mathbf{C}_\mathrm{e})^{-1}\mathbf{P}\mathbf{C}_\mathrm{o} \\ &= (\mathbf{C}_\mathrm{o}^{-\mathbf{1}} + \mathbf{P}^T\mathbf{C}_\mathrm{e}^{-\mathbf{1}}\mathbf{P})^{-1}.\end{aligned} \tag{4.10}$$

For the special case where $\mathbf{C}_\mathrm{o} = \sigma_\mathrm{o}^2\mathbf{I}$ and $\mathbf{C}_\mathrm{e} = \sigma_\mathrm{e}^2\mathbf{I}$, $\mathbf{C}_\epsilon$ reduces to

$$\begin{aligned}\mathbf{C}_\epsilon &= \sigma_\mathrm{o}^2\mathbf{I} - \sigma_\mathrm{o}^2\mathbf{P}^T(\sigma_\mathrm{o}^2\mathbf{P}\mathbf{P}^T + \sigma_\mathrm{e}^2\mathbf{I})^{-1}\mathbf{P}\sigma_\mathrm{o}^2 \\ &= (\mathbf{I}/\sigma_\mathrm{o}^2 + \mathbf{P}^T\mathbf{P}/\sigma_\mathrm{e}^2)^{-1}.\end{aligned} \tag{4.11}$$

The form (4.11) will be used in the simulations presented below in this chapter. Each diagonal element in $\mathbf{C}_\epsilon$ corresponds to the variance of the estimation error of one element in $\mathbf{o}$.

From Eq. (4.11) we can see that if (the norm of the) matrix $\mathbf{P}$ is large then the expected error will become small. As can be seen from Eq. (4.1) the elements in $\mathbf{P}$ is formed by convolutions with the input signals and, hence, a small error can be achieved by simply increasing the amplitudes of the input signals. The input signals are, however, limited in amplitude and length by the hardware used. Here we assume that the signal's length are L_u samples and the amplitudes are restricted to the interval $[-u_{\max} \leq u_i \leq u_{\max}]$. The criterion we have chosen to optimize is the sum over the diagonal elements in $\mathbf{C}_\epsilon$ (the trace),

$$\begin{aligned}\hat{\mathbf{u}} = \ &\arg\min_{\mathbf{u}} \ \mathrm{tr}\{\mathbf{C}_\epsilon\} \\ &\text{subject to} \quad |u_i| \leq u_{\max} \forall i.\end{aligned} \tag{4.12}$$

Note that the criterion (4.12) is non-quadratic and we may have many local minima. Here we have used genetic optimization to find good input signal candidates.

4.5 Simulation Examples

In this section a few examples are shown were a 16 element array with 0.9 mm wide elements and an array pitch of 1 mm has been simulated for different sets of control points and lengths

of the input signals. The array elements have center frequency of 3.5 MHz corresponding to a wavelength of $\lambda \approx 0.4$ mm in water. Figure 4.2(a) shows the optimized input signal for the 1st array element and Figure 4.1(b) shows the corresponding simulated wavefield snapshot.

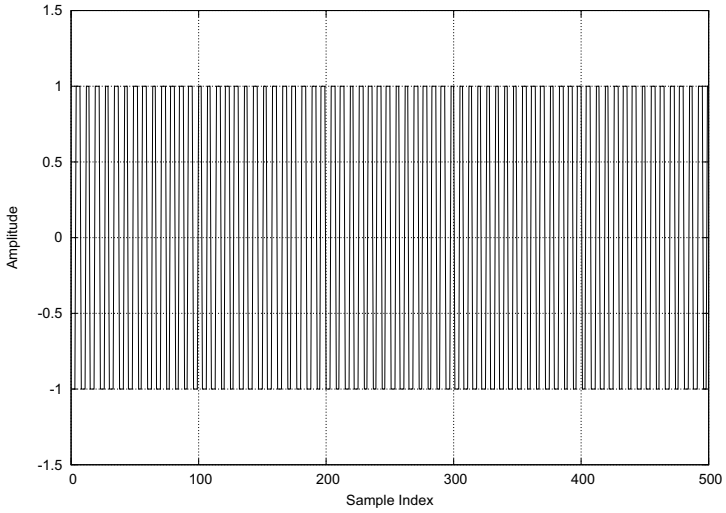

Figure 4.1: Input signal for element 1.

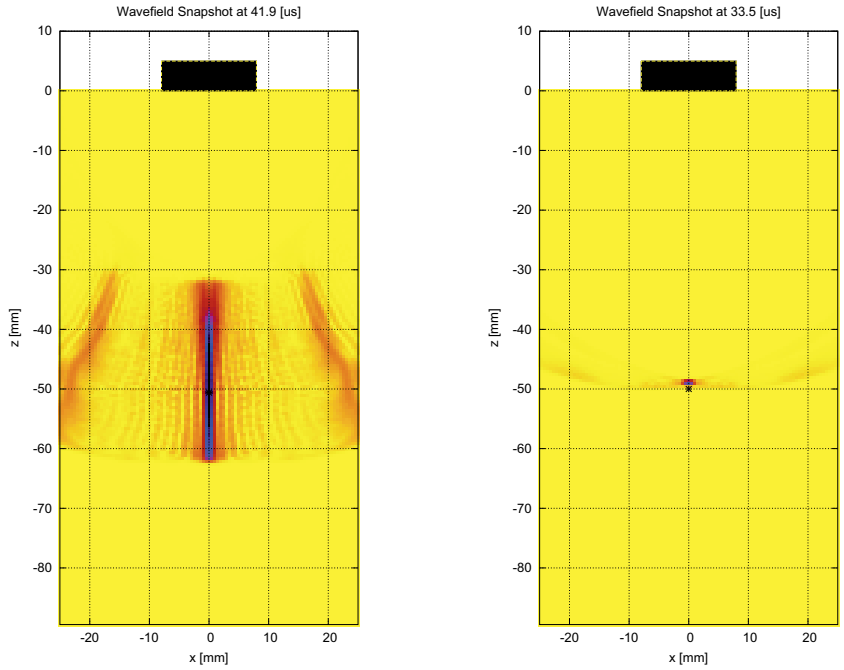

(a) Wavefield snapshot at $t = 41.9\mu$s.

(b) Wavefield snapshot for a traditionally focused array at $t = 33.5\mu$s.

Figure 4.2: 16 element array (with 0.9 mm wide elements and an array pitch of 1 mm) with $L_u = 500$ samples long input signals optimized for a single observation point at $x = 0$ mm, $z = -50.6$ mm.

For comparison, a simulated snapshot with traditional focusing is also shown in Figure 4.2(c). One can first note that u_i is always equal to $\pm u_{\max}$ and second, it is evident that by using the optimized input signals the acoustic power will be high for a substantially longer time duration

compared to using traditional focusing.

In Figure 4.3, an example with 4 relatively closely spaced control points using two different signals length are shown.

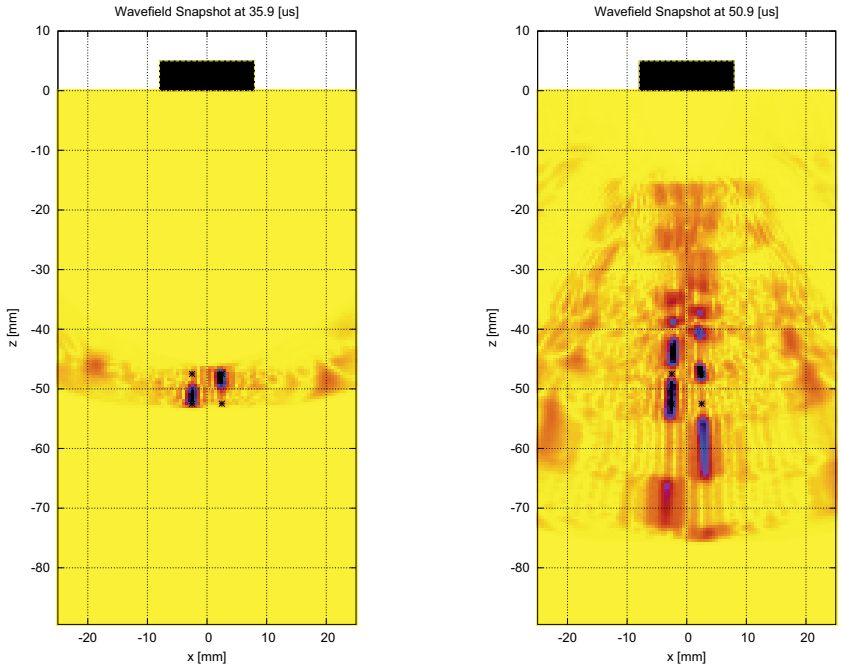

(a) Input signal length $L_u = 100$ samples. (b) Input signal length $L_u = 1000$ samples.

Figure 4.3: Wavefield snapshots with input signals optimized for four control points at: $(z = -47.5, x = -2.5)$ mm, $(z = -47.5, x = 2.5)$ mm, $(z = -52.5, x = -2.5)$ mm, and $(z = -52.5, x = 2.5)$ mm.

Figure 4.3(a) shows a wavefield snapshot for an input signal length of $L_u = 100$ samples and Figure 4.3(b) shows the corresponding snapshot for a length of $L_u = 1000$ samples. ¿From Figure 4.3(a) one can observe that the energy for control points at the same depth is always low for one control point and high for the other and as time evolves the energy at all control points will be high at some time instant.

In Figure 4.4 two more complex examples are shown. Figure 4.4(a) shows an example with six horizontally located control points and one can observe that a multi-beam field is obtained were most of the energy is concentrated around the control points. The example shown in Figure 4.4(b) has a relatively large number of control points. Here, a more diffuse field is obtained insonifying the total region of control points. One can note that most of the energy is concentrated directly under the array. The reason for this behavior is probably due to the fact that since the array elements have a non-negligible beam directivity the array system is most sensitive for scattering occurring directly under the array aperture. Sending more acoustic energy outside the array aperture will then probably increase the reconstruction error for the particular noise level used here. A lower noise level or longer input signals would probably result in a more evenly spread acoustic field.

4.6 Conclusions

In this chapter a novel method for input signal design in ultrasonic array imaging has been introduced. The new method is capable of optimizing the input signals in such way that the

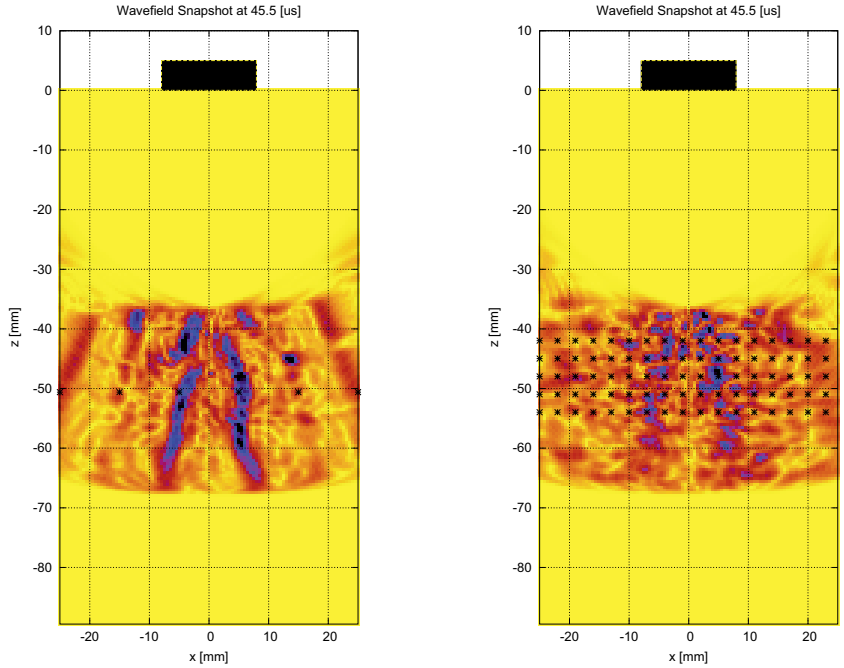

(a) Six control points horizontally aligned at $z = -50.6$ mm

(b) 85 control points uniformally located at $-54 < z < -42$ mm,$-25 < x < 25$.

Figure 4.4: Wavefield snapshots at $t = 45.5\mu$s with $L_u = 500$ samples long input signals.

scattering strengths at arbitrarily chosen control points can be estimated by using a linear minimum mean squared estimator with as low error as possible. This allows very fast imaging systems where the scattering amplitudes in large region-of-interests can be estimated using very few transmissions.

Bibliography

[1] F. Lingvall, T. Olofsson, and T. Stepinski. Synthetic aperture imaging using sources with finite aperture: Deconvolution of the spatial impulse response. *Journal of the Acoustical Society of America*, 114(1):225–234, July 2003.

[2] F. Lingvall. A method of improving overall resolution in ultrasonic array imaging using spatio-temporal deconvolution. *Ultrasonics*, 42:961–968, 2004.

[3] F. Lingvall and T. Olofsson. Statistically motivated design of input signals for ultrasonic array imaging. *2006 IEEE Ultrasonic Symposium*, pages 144–147, 2006.

[4] F. Lingvall and T. Olofsson. Statistically motivated design of input signals for modern ultrasonic array systems. *JASA*, 123, 2008.

[5] S.M. Kay. *Fundamantals of Statistical Signal Processing: Estimation Theory*, volume I. Prentice Hall, 1993.

ISSN 1404-0344
CM Gruppen AB, Bromma, 2008